A Numerical Study of Gas and Particle Flows in the Aerosol Deposition Process

Ali Zabihi Yeganeh

A Thesis

In

The Department

Of

Mechanical, Industrial and Aerospace Engineering

Presented in Partial Fulfillment of the Requirements
for the Degree of Master of Applied Science (Mechanical Engineering) at
Concordia University
Montreal, Quebec, Canada

Winter 2019

Concordia University

CONCORDIA UNIVERSITY
School of Graduate Studies

This is to certify that the thesis prepared

By: Ali Zabihi Yeganeh

Entitled: A Numerical Study of Gas and Particle Flows in the Aerosol Deposition Process

and submitted in partial fulfillment of the requirements for the degree of

Master of Applied Science (Mechanical Engineering)

complies with the regulations of the University and meets the accepted standards with respect to originality and quality.

Signed by the final examining committee:

_____ Chair

R. Sedaghati

_____ Examiner

B. Vermiere

_____ Examiner

S. Li

_____ Thesis Supervisor(s)

A. Dolatabadi

_____

C. Moreau

Approved by _____

Chair of Department or Graduate Program Director

_____

Dean,

Date _____

Abstract

Aerosol deposition is an emerging coating process for solid state deposition of ceramic particles at room temperature. The industrial applications for aerosol deposition method are MEMS, fuel cells, optical devices and RF components. During deposition, various parameters play influential roles such as nozzle geometry, powder size and material, pressure inside the deposition chamber and carrier gas pressure. Two different drag expressions for the particle phase modeling are proposed and compared in order to capture the physics governing the fluid-particle flow in partial vacuum conditions. Then, the main focus is dedicated to the effect of three-dimensional analysis, gas flow rate and substrate location on the gas flow and particle condition upon impact on the substrate. Numerical study is performed using a two-way coupled Eulerian-Lagrangian model for a slit sonic nozzle with various gas flow rates and standoff distances. Locations of the predicted shocks for the free jet case are validated against the theoretical and experimental studies in the literature. By placing a substrate in the computational domain at various standoff distances, the characteristics of gas flow, bow shock and importantly particle trajectories and conditions upon impact have been examined rigorously. Accordingly, the optimized model to predict particles velocity are proposed and the effect of different parameters on particles velocity during the spray and upon impact are discussed.

Acknowledgements

Hereby I would like to express my sincere gratitude to Professor Ali Dolatabadi and Professor Christian Moreau for their continuous helps and contributions in this research. This research definitely would not be possible without their dedication and support.

Special thanks to my beloved wife; Panteha and my family for their inspirations and emotional supports that always motivates me in life to pursue my dreams. At the end, I am very thankful to my dear friends Dr. Mehdi Jadidi and Saeed Garmeh for their helps and technical supports whenever problems encountered.

Table of Contents

List of Figures

Chapter 1

List of Tables

Chapter 1

Chapter 2

Chapter 3

List of symbols

A	Cross sectional area	$[m^2]$
c	Specific heat	$\left[{}^{J}/_{kg\,.\,K}\right]$
C_D	Drag coefficient	
D	Particle diameter	$[m]$
E	Internal energy	[J]
F_b	Body force per unit mass of particles	$\left[{}^{N}/_{kg}\right]$
F_D	Drag force	[N]
g	Gravitational acceleration	$\left[{}^{m}/_{s^2}\right]$
K	Thermal conductivity	$\left[{}^{W}/_{m\,.\,K}\right]$
k	Turbulence kinetic energy	$\left[{}^{J}/_{kg}\right]$
Kn	Knudsen number	
m	Mass	[kg]
Ma	Mach number	
n	Number of density	
Nu	Nusselt number	
p	Pressure	[Pa]
Pr	Prandtl number	
q	Heat flux	$\left[{}^{W}/_{m^2}\right]$

R_g	Universal gas constant	$\left[{}^{\mathrm{J}}/_{\mathrm{kg.\,K}}\right]$
Re	Reynolds number	
s	Molecular speed ratio	
t	Time	[s]
T	Temperature	[K]
T^*	Non-dimensional temperature	
u	Velocity vector	$[{}^{\mathrm{m}}/_{\mathrm{s}}]$
y^*	Non-dimensional temperature from the wall	

Greek symbols

Γ	Particle flux	$[{}^{1}/_{\mathrm{s}}]$
γ	Specific heat ratio	
ε	Turbulence dissipation rate	$\left[{}^{\mathrm{J}}/_{\mathrm{kg\,.\,s}}\right]$
λ	Mean free path	[m]
μ	Dynamic viscosity	$\left[{}^{\mathrm{kg}}/_{\mathrm{m\,.\,s}}\right]$
ρ	Density	$\left[{}^{\mathrm{kg}}/_{m^3}\right]$
σ	Molecular diameter	[Å]
τ	Deviator stress tensor	
υ	Kinematic viscosity	$\left[{}^{\mathrm{m}^2}/_{\mathrm{s}}\right]$
Ω_{ω}	Collision integral	

1. Introduction

Overview

In this chapter, a brief introduction to thermal spray processes is provided and a specific description of aerosol deposition technology is presented. Moreover, different parts of aerosol deposition and their roles in the deposition process are explained in detail. At the end, objectives and significance of this work are presented.

1.1. Overview of cold spray coating process

Cold spray refers to the group of coatings where a stream of ductile particles is deposited into a prepared substrate. Upon impact a bond forms between the new incoming particle and the surface causing a coating build-up until it reaches the final thickness. In this process, the operating temperature is lower than the melting point of the particles; therefore, in this method, oxidation is eliminated and the final coating is highly dense and has fewer voids and cracks. In this process, solid state particles adhere to the surface because of their high kinetic energy upon impact that creates plastic deformation. In the cold spray process a compressed gas is accelerated by a converging-diverging nozzle discharging to deliver the particles to the substrate. Upon impact, usually there is a significant bow shock near the substrate that decelerates the particles. During the process, a residual stress is created due to the impact of the particles [1]. Figure 1.1 shows the schematic of a cold spray system.

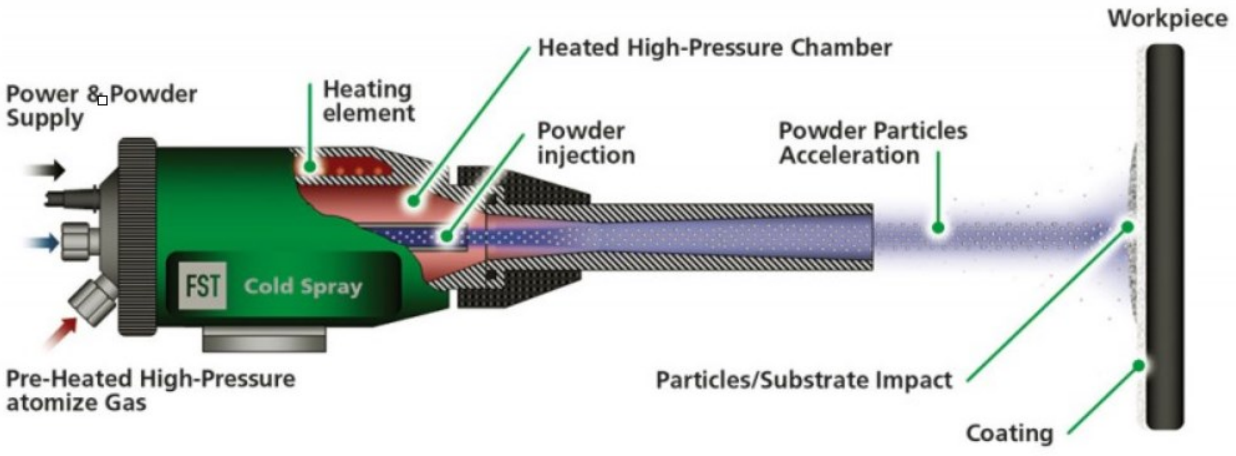

Figure 1.1 Schematic of cold spray system [2]

The earliest invention in cold spray process was done by Alkhimov et al. in 1980's in the Soviet Union. In this method, particles are accelerated in an unheated gas flow in the range of 650 m/s – 1200 m/s to be deposited on the substrate. Later, they added a mixing chamber powder feeder and rectangular supersonic nozzle working with the preheated gas-powder mixture [3]. Continuous improvement of cold spray technology is about to reduce oxidation during the process. In the latest version of cold spray technology, the oxidation is eliminated due to the elimination of particles melting. However, for a high number of passes, oxidation is unavoidable due to the local melting of metallic particles during impact. Schmidt et al. [4] illustrated this phenomenon by explaining the adiabatic shear instability for deposition of metallic ductile particles in cold spray process. Oxidation results in poor bonding between different layers [4].

Cold spray method is limited to ductile materials and for the ceramic particles conventional methods are still using molten or semi molten particles in high operating temperature causing the oxidation in the coating and also limits the process for only certain substrate materials that can tolerate high temperatures; therefore, to create dense ceramic coating for different substrate materials a recent method called aerosol deposition spray is introduced [3, 5, 6]. This method is explained comprehensively in this chapter including the industrial application and the history of the process.

1.2. Aerosol deposition spray process

In aerosol deposition (or so called vacuum cold spray), despite the cold spray process, deposition happens in a near vacuum condition instead of atmospheric conditions; therefore, each system contains a mechanical pump and a deposition chamber. Operating pressure inside the deposition chamber is usually between 0.1 – 15 torr and the pressure inside the aerosol chamber varies between 0.06 – 1 atm, depending on the gas flow rate and nozzle geometry. The difference

between pressure inside the aerosol chamber and deposition chamber causes acceleration of particles through the nozzle in order to reach adequate velocity for bonding. There is a unique flow rate for each pressure difference, so one way to control the process is having control over the gas flow rate. For this purpose, a gas flow rate controller has been introduced to the system for controlling the carrier gas flow rate. Moreover, the nature of the gas is also another key parameter in this process. For instance; Air, Nitrogen, Argon and Helium are some of the common gases that have been used so far in the aerosol deposition process. In order to avoid the agglomeration of particles inside the aerosol chamber, an aerosol generator is utilized to create vibration and facilitate the mixing process of particles and the carrier gas to create the aerosol. Finally, the aerosol goes through a nozzle to spray particles on the substrate with adequate velocity [5, 7–10]. Figure 1.2 shows the schematic of a typical aerosol deposition system including all the components.

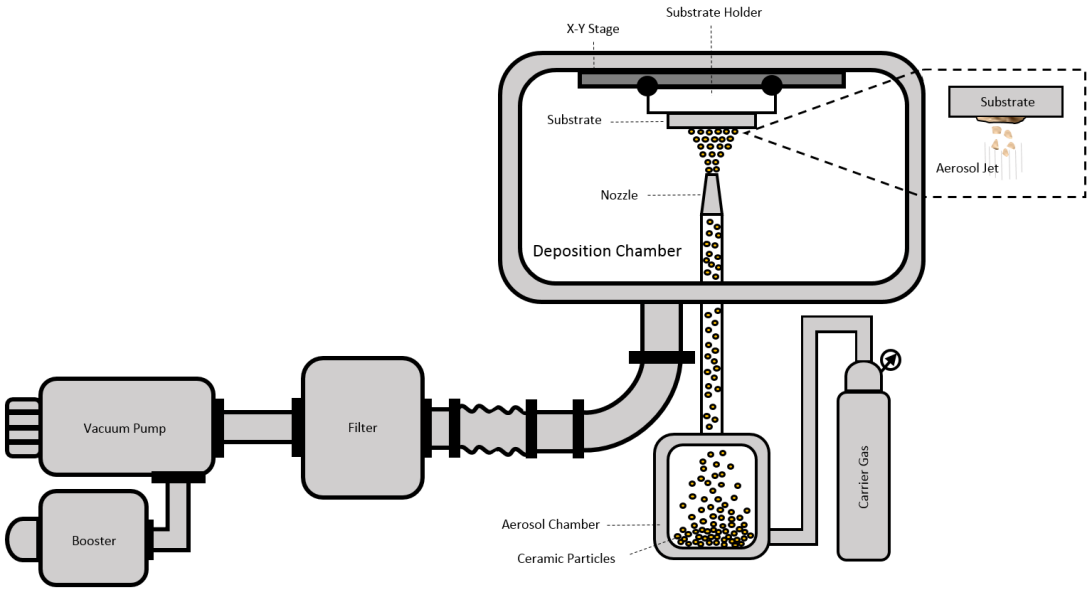

Figure 1.2 Schematic of aerosol deposition system

The in-flight particles behaviour during their travel inside the nozzle to the substrate is important to understand and can change the coating properties. Interaction between the particles and shocks in this region can decelerate the particles velocity. Therefore, the nozzle geometry has a significant influence on the process. The most widely used geometry for this process to accelerate particles is a slit nozzle with the rectangular cross sectional area of $0.4 \times 10\ mm^2$, while in some cases supersonic nozzles have been used in order to reach higher velocity of the particles [5, 6, 8, 11, 12].

Although many parameters can affect the coating formation, the final part can be significantly influenced by manipulating the mass flow rate, pressure inside the vacuum chamber, standoff distance, nozzle geometry, particles material and size distribution. Each of these parameters directly and indirectly affects the in-flight particles behaviour including their trajectory and velocity leading to different kinetic energy and particles velocity upon impact [6, 13–16].

1.3. Applications and bonding mechanism of aerosol deposition

Fabrication of ceramic coatings by conventional thermal spray methods involves high operating temperatures. This temperature increase can change the mechanical and optical properties of materials. For instance; alumina at room temperature is in α phase. In case of rapid solidification, α-alumina can change to γ-alumina which is much less wear resistant. Therefore, it is desirable to have a process at room temperatures to maintain the initial properties of the powder. Also due to the high operating temperature for thermal spray methods, it is difficult to apply them on low melting point materials such as metals, polymers and plastics. In industry, fabrication of display devices, fuel cells, optical devices microelectromechanical systems (MEMS) and RF components depends highly on operating temperatures of the process. The quality of the coating regarding the density of the coating and also the adhesion between each

layers are important elements for industrial applications. The most recent method to create fully dense ceramic coatings is aerosol deposition process, also known as the vacuum cold spray and the vacuum kinetic spray method. In this method, coated layers are fully dense due to the low temperature and high impact velocity of fine ceramic particles on the substrate. Although the principle behind the bonding mechanism of this method has not been clarified yet, studies show that particle's kinetic energy is converted into thermal energy during the impact and plays a key role in the process. This thermal energy creates high temperature at the impact location, which can create local melting of the substrate but not high enough to melt the ceramic particles resulting in the adhesion between the ceramics and substrate and creating a highly dense coating with minimum cracks between layers compared with conventional methods. To create a high quality coating, the kinetic energy of the particles plays a significant role and it depends on the impact velocity and particle size distribution[1–5].

Compared with the cold spray technology for metallic coatings, in aerosol deposition technology brittle ceramic particles differentiates the fundamental of the process; therefore, instead of adiabatic shear stress in cold spray, which causes the bonding between the metallic particles and the substrate, fracture of ceramic particles and local increase of temperature causes the adhesion and coating buildup in the aerosol deposition process [3], [4].

Abrasive features of the ceramic particles makes this method complicated and results in a narrow window of deposition compared with the cold spray process, high velocity impact can result in erosion, while low velocity impact cannot create a coating due to the low kinetic energy. These phenomena can be seen in Figure 1.3 presenting the window of deposition for aerosol deposition process and cold spray process [5].

Figure 1.3 illustrates the comparison between the window of deposition for Aerosol Deposition (AD) and Cold Spray (CS) processes.

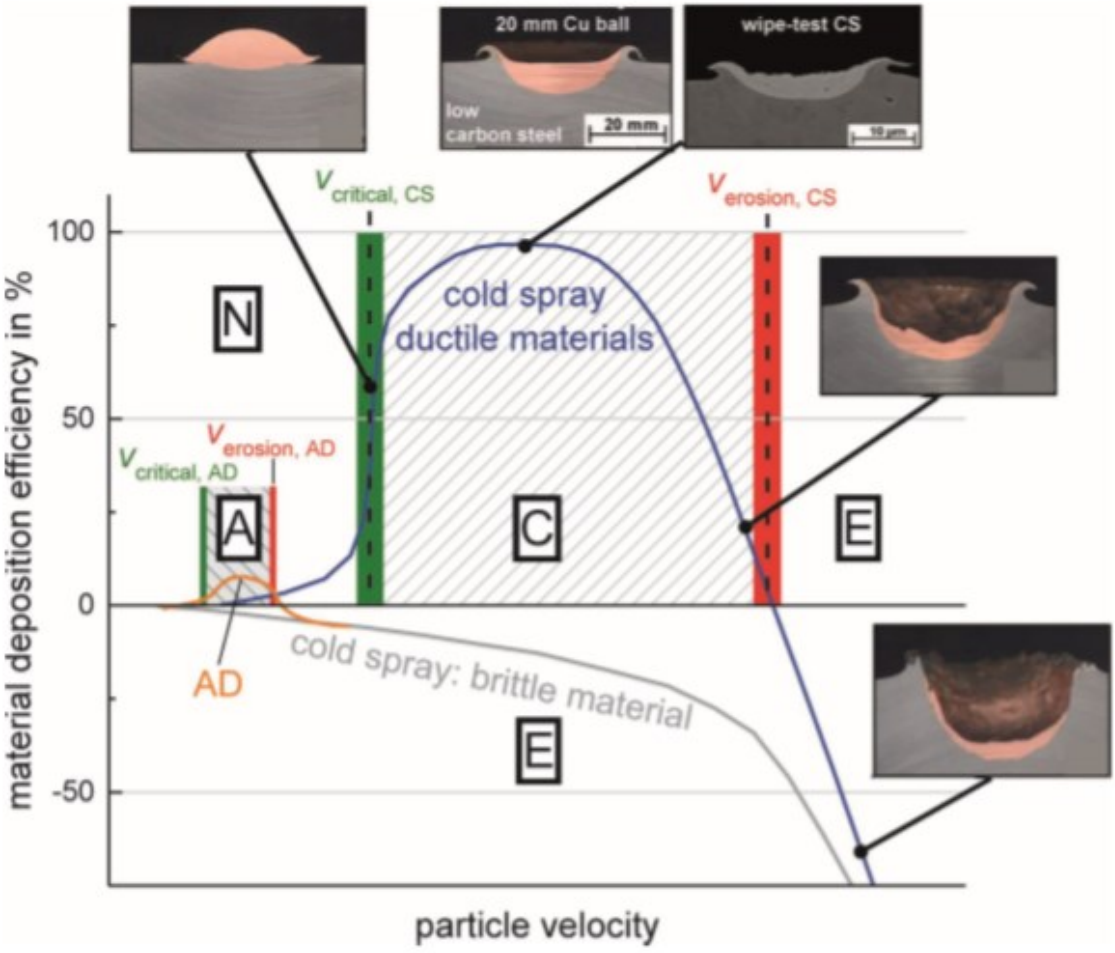

Figure 1.3 Window of deposition for cold spray and aerosol deposition processes
AD: Aerosol Deposition, CS: Cold Spray [5]

In addition to the effect of impact velocity, particle size distribution and degree of agglomeration have a significant influence on the process. Large particles have higher kinetic energy result in the same erosion rate as high impact velocity. For agglomerated particles, kinetic energy causes deagglomeration of the particle instead of adhesion and create a porous coating with low adhesive strength. On the other hand, small particles cannot pass the bow shock at the location

of the substrate and even if they pass, they do not have enough energy to create strong bonding with the substrate or sub layers. These facts can be seen in Figure 1.4 [5], [17].

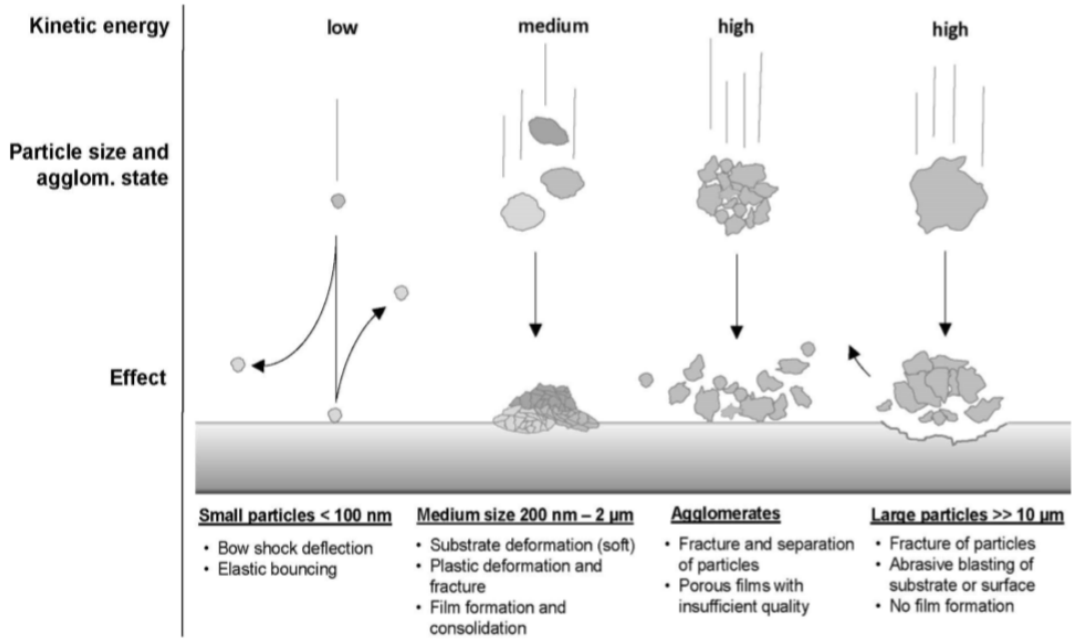

Figure 1.4 Effect of particles size and degree of agglomeration on deposition process [2]

1.4. Vacuum physics

Below atmospheric pressure, transport phenomena are dependent on the vacuum pressure, hence; attention to the properties of the gas in the vacuum condition is a vital point in the study of vacuum science technology. By reducing the pressure from atmospheric to high vacuum condition, the chance for molecular collision will reduce. The reason behind this fact is the reduction in the population of gas molecules that increase the distance between the molecules with each other or with the walls of the container. In order to define the level of vacuum quantitatively, mean free path and physical length are introduced to make a correlation between the pressure of the physical domain and the flow region. Equation 1-1 shows that mean free path is a pressure dependent property because of the dependency of the gas density to the pressure

[18]. Where, λ is the meanfree path, d_0 is the diameter of the gs molecules and n is the number of density.

$$\lambda = \frac{1}{\sqrt{2}\pi {d_0}^2 n} \tag{1-1}$$

Table 1-1 shows the properties of air for different range of the vacuum pressures at room temperature ($T = 22$ ℃), where d′ is the average molecular spacing, T is the temperature in Kelvin, m is the particles mass and Γ is the particle flux.

Pressure (Pa)	n (m^{-3})	d′ (m)	λ (m)	Γ $(m^{-2}.s^{-1})$
1.01×10^5 (760 Torr)	2.48×10^{25}	3.43×10^{-9}	6.50×10^{-8}	2.86×10^{27}
100 (0.75 Torr)	2.45×10^{22}	3.44×10^{-8}	6.60×10^{-5}	2.83×10^{24}
1 (7.5×10^{-3} Torr)	2.45×10^{20}	1.60×10^{-7}	6.60×10^{-3}	2.83×10^{22}
10^{-3} $(7.5 \times 10^{-6} Torr)$	2.45×10^{17}	1.60×10^{-6}	6.64	2.83×10^{19}
10^{-5} $(7.5 \times 10^{-8} Torr)$	2.45×10^{15}	7.41×10^{-6}	6.64×10^2	2.83×10^{17}
10^{-7} $(7.5 \times 10^{-10} Torr)$	2.45×10^{13}	3.44×10^{-5}	6.6×10^4	2.83×10^{15}

Table 1.1 Low pressure properties of Air at 22 ℃ [18]

This particle flux is directly proportional to the square root of temperature based on equation 1-2 which means that by increasing temperature, the energy of the molecules and subsequently, the collision rate within the molecules of the gas increases [18].

$$\Gamma = n\left(\frac{kT}{2\pi m}\right)^{1/2} \tag{1-2}$$

In aerosol deposition technology process happens in room temperature, so the properties of the gas are mainly a function of pressure.

In general, the flow regions in vacuum science divides into three different regions described by a non-dimensional parameter called the Knudsen number. The Knudsen number is the ratio of mean free path to the characteristic dimension of the system and in aerosol deposition technology, the characteristic length is assumed to be the smaller side wall thickness of the nozzle throat for the gas phase analysis, but for circular nozzles this term can be simply considered as the diameter of the throat [18, 19].

$$Kn = \frac{\lambda}{d} \tag{1-3}$$

For the continuum assumption, the diameter of the throat should be much larger than the mean free path; therefore, the collision rate of the gas molecules is significant and the flow is categorized as viscous continuous flow. When the mean free path is equal or greater than the nozzle throat, the concept of the viscosity becomes meaningless because of the more collision of the molecules with the wall boundaries instead of themselves. This region is called the molecular flow region that happens usually in high vacuum systems where the mean free path is large compared with the dimensions of the system. At the end, there is a region that the flow is neither molecular nor viscous which is called transitional flow. Table 2-2 shows the relation between the Knudsen number and the flow regions [19]. In aerosol deposition technology, the process happens usually in 1 torr and above while some experiments have been done so far below this range. Therefore, the gas phase is located in the continuum region.

Knudsen number	Flow region
$Kn \leq 0.01$	Continuum
$0.01 < Kn < 1$	Transient
$Kn \geq 1$	Molecular

Table 1.2 Different flow regimes based on Knudsen number

1.4.1. Density

For the operating range of pressure in aerosol deposition process, the gas is dilute and consist of a large number of molecules with the chaotic motions. The only significant force acting on the molecules are the elastic collisions with each other, so the gas is considered as an ideal gas and the density is calculated from equation 2-4, where P is the absolute pressure, R is the gas constant and T is the absolute temperature [20].

$$\rho = \frac{P}{RT} \tag{1-4}$$

1.4.2. Viscosity

The viscosity term for a gas defines the viscous force when the gas undergoing shearing motion. This force is the result of the momentum difference between the molecules, which means that it acts like a frictional force. In vacuum science, viscosity is merely the result of momentum transfer between the molecules due to the reduction of molecular collisions. Here instead of the classical approach, kinetic theory predicts that viscosity is independent of density and proportional to the square root of the absolute temperature and molecular mass [18]. From the kinetic theory, gas molecules are considered as hard spheres; therefore, the viscosity also

decreases as the square of the molecular diameter. It should be noted that this theory is only valid for a limited range of pressures. In a medium vacuum condition (e.g. less than 10^{-3} Torr), the viscous force will be eliminated due to the elimination of molecular collision and momentum transfer mechanism [18, 21].

To summarize, kinetic theory is valid only when the physical length is equal or greater than the mean free path [18]. Viscosity is calculated by equation 1-5, where μ is the viscosity in units of kg/m.s, T is the absolute temperature in units of Kelvin, σ is the molecular diameter in units of Angstroms and Ω_ω is the collision integral reported in an empirical term with the dimensionless temperature [21], [22]. In equation 1-6, T^* is the dimensionless temperature, k is the Stephan Boltzmann constant and ϵ is the minimum pair-potential energy; where σ and ϵ/k are known as Lennard-Jones parameters [23].

$$\mu = 2.67 \times 10^{-6} \frac{\sqrt{M_\omega T}}{\sigma^2 \Omega_\mu} \tag{1-5}$$

$$T^* = \frac{Tk}{\epsilon} \tag{1-6}$$

1.4.3. Thermal conductivity

Kinetic theory explains heat conductivity in the same manner as viscosity and based on this theory, it is independent from pressure if the mean free path is smaller than the physical dimensions. The thermal energy in the gas transfers by the collision of the molecules; therefore, at very low pressures when mean free path is much greater than the physical dimensions, heat transfer is the result of the collision between the molecules with wall boundaries of the physical domain instead of each other and kinetic theory is no more valid in this condition. While in the

aerosol deposition process, the Knudsen number is less than 0.01 and the kinetic theory can be used for the thermal conductivity same as viscosity [18].

According to equation 2-6, thermal conductivity is calculated based on kinetic theory, where R is the universal gas constant, M_ω is the molecular weight, μ is the viscosity and C_p is the specific heat [23].

$$k = \frac{15}{4}\frac{R}{M_\omega}\mu\left[\frac{4}{15}\frac{C_p M_\omega}{R} + \frac{1}{3}\right] \quad (1\text{-}7)$$

1.5. Physics of highly under-expanded flows

When a high pressure gas is exhausted into an area with low pressure like a vacuum chamber, the jet expands rapidly into that area by increasing the cross section of the jet and creating a strong normal shock known as a Mach disk. A schematic of this physical phenomenon is displayed in Figure 1.5 showing a highly under-expanded jet [24]. The flow is subsonic right after the Mach disk. The flow behind this reflected shock is still supersonic, where the second normal shock can happen similar to the first one as shown in Figure 1-5. The location and diameter of first Mach disk is a function of pressure ratio and diameter of the nozzle's exit. Due to the importance of the in-flight particles velocity and trajectory in aerosol deposition process, prediction of Mach disk location is important. Shocks location can change the coating structure by affecting the in-flight particles velocity and trajectory.

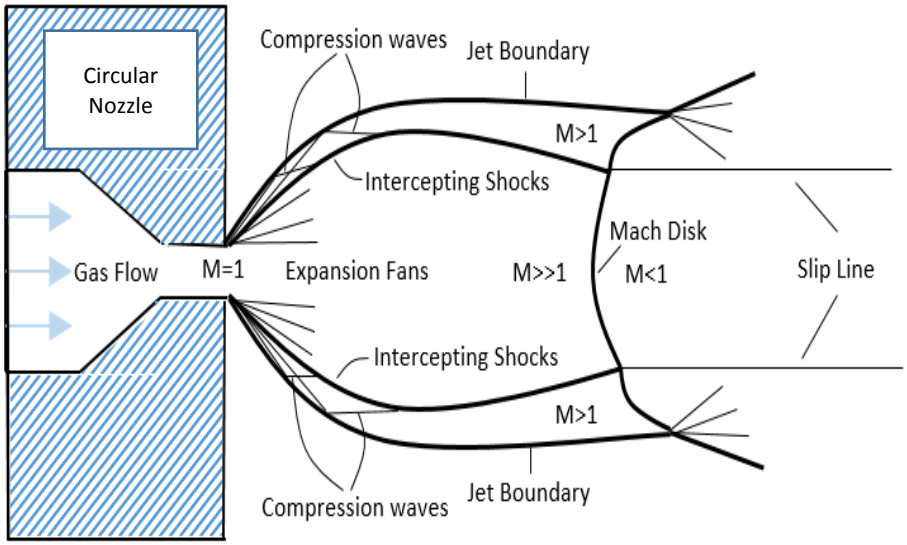

Figure 1.5 Schematic of a highly under-expanded jet

The Mach disk location and the Mach number associated with the distance from nozzle exit is presented based on the pressure ratio for the pressure inlet from 150 – 15000 psia and pressure outlet from atmospheric to 0.1 torr. The stagnation temperature also varies from 300 – 4200 K for different gases such as Nitrogen, Argon, Helium, Helium-Argon mixture, Carbon-dioxide and Freon 22 [24].

The nozzles associated with this study were circular converging nozzles and the exit diameter ranged from 0.026 to 0.119 in. The Mach disk location can be obtained from figure 1.6 which shows the relation between the pressure ratio and non-dimensional Mach disk distance from the nozzle exit plane [24].

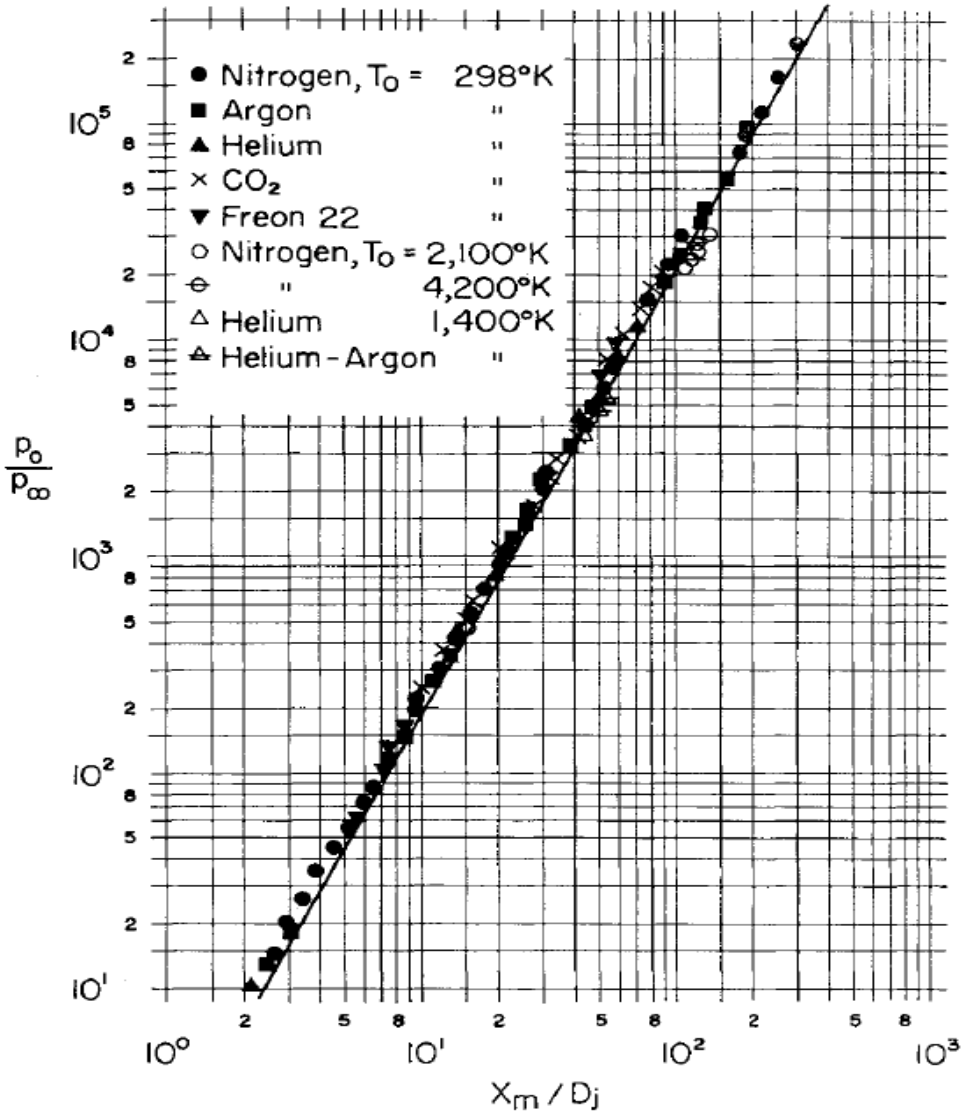

Figure 1.6 Relation between the pressure ratio and non-dimensional Mach disk distance [24]

The relation between the Mach number upstream of the shock for the non-dimensional distance associated with that is also presented in Figure 1.7 for different specific heat ratios of the gas.

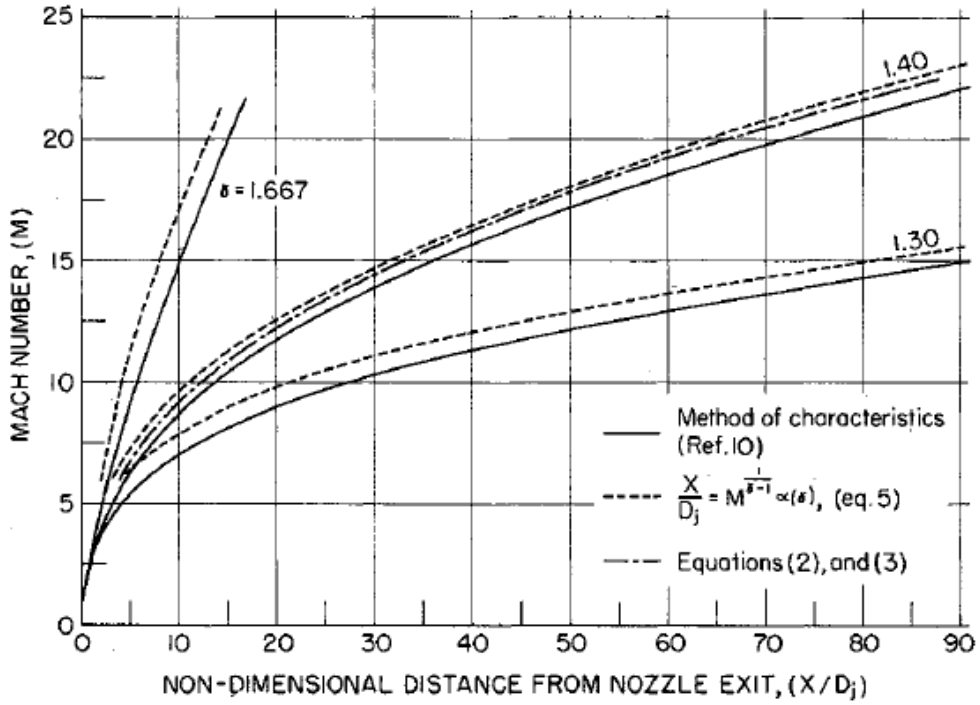

Figure 1.7 Relation between the Mach number upstream of the shock and non-dimensional distance [24]

From Figure 1.6, the correlation between pressure ratio and non-dimensional Mach disk location for different gases is as follow.

$$\frac{P_0}{P_\infty} \approx 2.4\left(\frac{X_m}{D_i}\right)^2 \tag{1-8}$$

Where, P_0 and P_∞ are the stagnation and back pressure, X_m is the Mach disk location and D_i is the diameter of nozzle exit [24].

1.6. Previous work in aerosol deposition spray

In 2001, Akedo and Takagi proposed a new method for deposition of fine ceramic particles to the substrate inside a vacuum chamber. This was the first version of an aerosol deposition system for creating highly dense ceramic coatings well below the particles melting point temperature

in order to preserve the microstructure properties of both substrate and coating material. During the same year, Akedo and Lebedev studied the influence of the carrier gas on electrical and optical properties of $Pb(Zr,Ti)O_3$ coating. They found that the carrier gas has a significant influence on the transmittance value of PZT thin film and influence of carrier gas velocity on the ferroelectric properties. They concluded that these properties are related to the particles impact velocity [25]. In order to clarify the particles adhesion process, in 2006, Akedo did study on the mechanical properties of particles and their impact velocity using a compression test for single submicron particle and time-of-flight method to obtain the conditions upon impact for the later finite element method (FEM) impact analysis. Figure 1.8 shows the FEM simulation for the local temperature and pressure increase due to the impact of particle and substrate with the 300 m/s impact velocity [8].

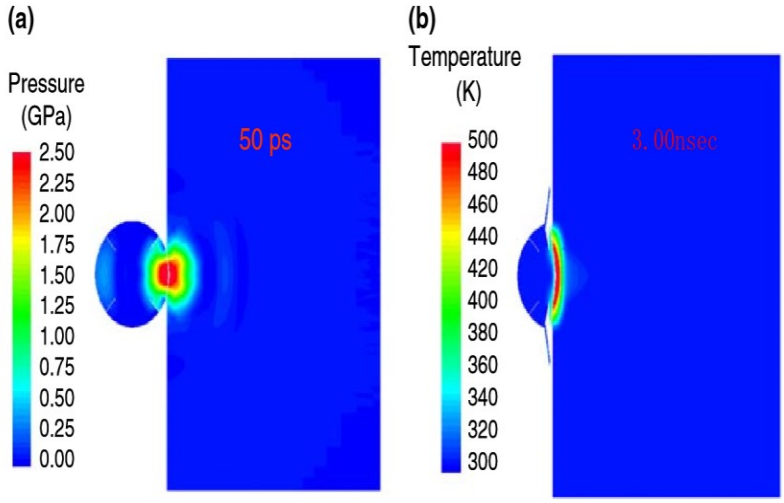

Figure 1.8 FEM simulation of local rise in temperature and pressure during impact [8]

In the same year, Akedo presented the relation between gas flow rate and particle velocity for different particles and different carrier gases. Figure 1.9 shows the relation between gas flow rate and particle velocity for the slit nozzle with cross section of $0.4 \times 10mm^2$. Air and Helium

were utilized as a carrier gases to spray Al_2O_3 and PZT powders and to determine the particle velocity upon impact, the time of flight method was utilized to precisely evaluate the velocity of the particles upon impact [6, 26].

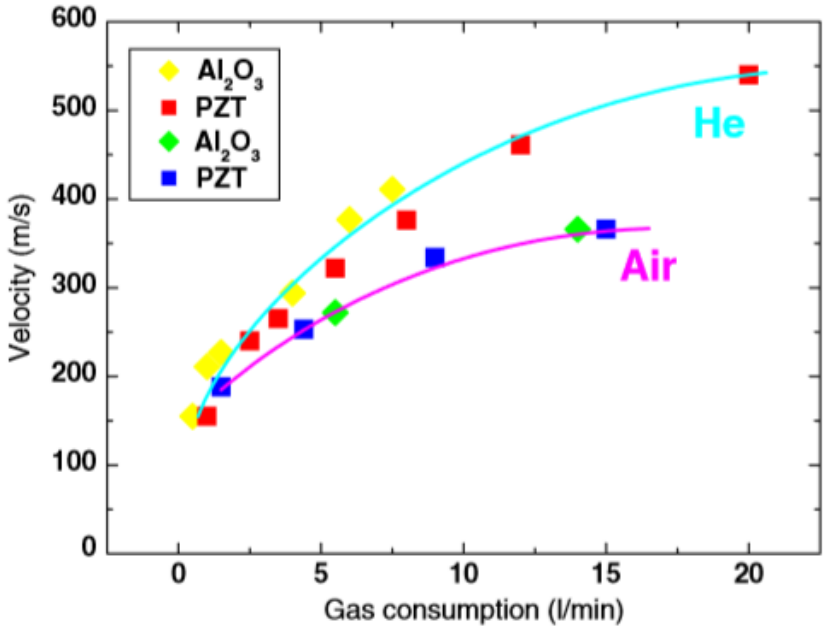

Figure 1.9 Relation between impact particle velocity and gas consumption [6]

In order to get control over the process, and also to estimate the particles trajectory and velocity magnitude, CFD studies has certain advantages for aerosol deposition technology, therefore, Katanoda et al. [27] performed a gas dynamic simulation of the aerosol deposition method to investigate the effect of carrier gas on particles during the spray. They presented the correlation between the gas velocity and particle velocity in aerosol deposition process. The two-dimensional, time-dependent form of the Navier-Stokes equations was used for the gas flow modelling. The stagnation pressure upstream of the nozzle was set to the constant values of 2 – 6kPa, while the back pressure, stagnation temperature and substrate location was fixed at 100 Pa, 300 K and 15mm, respectively. Finally, for the drag expression, Henderson's equation was

used in their study to calculate the inflight particles velocity [17], [27]. Later on, Park et al. [16] simulated and discussed the effect of the bow shock in aerosol deposition application by studying the effect of nozzle geometry and operating condition in the formations of the shocks. Finally, they concluded that by reducing the pressure inside the deposition chamber from $0.01316 - 1$ bar; nozzles with greater diverging angles are needed [15]. This was the earliest work in spray nozzle optimization for the aerosol deposition process that revealed the significant influence of the nozzle geometry on this process. Subsequently, in 2011, Lee et al. [11] studied the performance of supersonic nozzle flow in both experimental and numerical fields for aerosol deposition applications. They presented the effect of shockwaves, nozzle geometry, carrier gas viscosity and particle density using Fluent 6.3 CFD code for fully compressible Navier-Stokes equations. They concluded that nozzles with optimum condition; $P_e = P_{amb}$ provide maximum kinetic energy for the particles due to the reduction of shock formation leading to a uniform and void free coating [11].

Alongside the effect of carrier gas and nozzle geometry on particles velocity, other parameters such as particles size and material can drastically change the microstructure of final coating. Moreover, deposition efficiency and its correlation with the impact velocity were not clarified until 2013 that Naoe et al. [14] studied the relation between the impact particle velocity with the carrier gas consumption and deposition efficiency. They found that by increasing the carrier gas consumption, particles velocity will increase, but it will not necessarily increase deposition efficiency of the coating because of erosion that happens in higher impact velocity. This fact had been already mentioned earlier by Akedo et al. [7] and Hanft et al. [4]. Naoe et al. [14] investigated the effect of particles manufacturing process in deposition efficiency of aerosol deposition method. They found that with the same particle size distribution, sintered particles

have higher deposition rate compared to the one produced by Chemical Vapor Deposition (CVD) methods [5, 8, 13, 14].

Application of aerosol deposition process is not limited only in ceramic coatings. For instance, metallic alloys such as Fe-based alloys have been deposited by this method. Kwon et al. [28] studied the correlation between the carrier gas consumption and mechanical properties of Fe-based amorphous alloys with a vacuum kinetic spray method. They have concluded that in spite of ceramic coatings obtained from vacuum kinetic spray method, thickness of this coating is higher and proportional to the carrier gas consumption. They also showed that by increasing the carrier gas consumption, coating roughness will increase due to higher impact velocity. Their coating shows higher porosity compared with the non-porous ceramic coatings and by increasing the carrier gas consumption, porosity of the coating will increase. They concluded that from the mechanical properties point of view, increasing the gas flow rate will also increase the adhesive bonding strength of this coating while the cohesive bonding strength remains the same [28].

Park et al. [29] numerically and experimentally studied the effect of gas flow rate, agglomeration and particle size on the Al_2O_3 particles impact velocity. In this study, the Reynolds-averaged Navier Stokes (RANS) equations were used with the realizable $k-\varepsilon$ turbulence model. For the discrete phase modeling, they assumed that the particle phase is dilute compare with the gas phase so, the interaction of the particles with each other are negligible and Lagrangian approach can be utilized. For the particles dynamic, they assumed that the only existing force is the drag force and the spherical drag expression from ANSYS Fluent v.13 library is utilized in this work. They concluded that particles velocity are proportional to the flow rate. Moreover; smaller particles under 1μm have higher inflight velocity magnitude but, their impact velocity decrease

due to the bow shock effect at the substrate. Also the coating obtained from the sub-micron particles was very weak in terms of bonding strength. The effect of working distance is also reveals the relation between the film thickness, width of the coating and the standoff distance. They concluded that by increasing the standoff distance, film thickness decreases and width of the coating increases [29]. Johnson et al. [17] also did two-dimensional numerical study to predict a single particle velocity and trajectory for different particle sizes at 7.5 mm and 10 mm standoff distances. Fully compressible Navier-Stokes equations with the ideal gas assumption is utilized for the gas phase modelling and only one-way coupling of the gas phase to the dispersed-phase utilized due to the very low volume fraction assumption in this study. For particle tracking, the simplest high velocity drag correlation (Schiller-Naumann) is considered for the calculation of the drag force applied to the particles. They concluded that, larger particles could overcome the bow shock at the substrate location, while smaller particles below 0.5μm are distracted by the bow shock. Moreover, smaller particles have higher inflight velocity compare with large particles [16].

Along with the numerous experimental and numerical studies on the effect of flow rate, carrier gas and particle size distribution on particles inflight behaviour, there is some work that has been done to study some other parameters such as powder structure, substrate hardness and the correlation between the fracture mode of the particles and critical impact velocity to clarify this coating process [30, 31].

1.7. Objectives

The main motivation for the current study is to address the necessity of a numerical study to obtain a repeatable and controllable coating for different gas flow rates and standoff distances. The objectives are summarized below:

1. Study the effect of three-dimensional simulation on flow characteristics compared with the two-dimensional simulation.
2. Study the effect of gas flow rate and standoff distance on flow characteristics such as location of the shock, velocity magnitude and Mach number.
3. Investigating the effect of compressibility and rarefaction on in-flight particles behaviour.
4. Predicting the particles velocity upon impact in different conditions such as carrier gas flow rate, standoff distance and thermophoretic force effect.

2. Methodology

Overview

In this chapter, the fundamental physics of vacuum and governing equations for both continuous and discrete phase are presented. In addition, all the assumptions, boundary conditions and the reasons behind them are discussed in this chapter. This study includes solution for the continuous gas phase and then utilizes this solution for the discrete phase calculation with Eulerian-Lagrangian approach, where the volume fraction of the solid phase assumed to be less than 5 % compared with the gas phase.

2.1. Continuous phase governing equations

According to the physics of the process, continuous phase is considered as a viscous flow; therefore, Navier-Stokes equations are utilized for the continuous phase analysis. These equations are written as follow.

2.1.1. Mass conservation equation

The equation for conservation of mass, or continuity is written as follows.

$$\frac{\partial \rho}{\partial t} + \nabla \cdot (\rho \vec{v}) = S_m \tag{2-1}$$

Equation 2-1 is the general form of the mass conservation equation valid for both incompressible and compressible fluids. The added mass to the continuous phase from the discrete second phase is the source term shown by S_m in equation [23].

2.1.2. Momentum conservation equation

The general form of the momentum conservation equation for an inertial reference frame is described as follow.

$$\frac{\partial}{\partial t}(\rho \vec{v}) + \nabla \cdot (\rho \vec{v} \vec{v}) = -\nabla \mathrm{p} + \nabla \cdot (\bar{\bar{\tau}}) + \rho \vec{g} + \vec{F} \tag{2-2}$$

Where p is the static pressure, $\bar{\bar{\tau}}$ is the stress tensor described in equation 2-3, $\rho \vec{g}$ is the gravitational force and $\vec{F}$ is the external body forces. For instance, a common external forces that exist in spray processes is the force arises from the interaction of dispersed phase and continuous phase.

$$\bar{\bar{\tau}} = \mu \left[(\nabla \vec{v}^T) - \frac{2}{3} \nabla \cdot \vec{v} I \right] \tag{2-3}$$

In equation 2-3, μ is the molecular viscosity, I is the unit tensor and the second term in the right hand side explains the changes in volume in case of volume dilation [23], [32].

2.1.3. Energy equation

The general form of energy equation is described as follow.

$$\frac{\partial}{\partial t}(\rho E) + \nabla \cdot \left(\vec{v}(\rho E + p)\right) = -\nabla \cdot \left[\sum_j h_j J_j\right] + S_h \quad (2\text{-}4)$$

Where, S_h is the energy source term and E in equation 2-11 is described as follow.

$$E = h - \frac{P}{\rho} + \frac{V^2}{2} \quad (2\text{-}5)$$

2.1.4. Equation of state

To complete the system of equations for the continuous phase and also to take the compressibility into account, the equation of state for ideal gas is utilized as follow.

$$p = \rho RT \quad (2\text{-}6)$$

2.2. Turbulence modeling

Due to the high pressure difference between the aerosol chamber and deposition chamber in aerosol deposition process, sudden expansion of the flow after the nozzle exit is unavoidable which causes acceleration of the flow and creating a large turbulent area. To create an acceptable prediction of the flow characteristic, a suitable turbulence model is necessary here.

According to the large computational cost associated with DNS and LES, RANS models have been used frequently in aerosol deposition spray simulation. Among the various models of RANS, RNG $k-\varepsilon$ and realizable $k-\varepsilon$ models have been used widely, due to their better performace compared with the standard $k-\varepsilon$ model for spray applications. This model is also

need less computational time compared with Reynolds stress models [15], [23], [29]. The realizable $k-\varepsilon$ turbulence model is utilized in this study.

In Reynolds averaging, the exact solution of Navier-Stokes equations are divided into two components. One is the mean component and the other is the fluctuating component. For instance, the velocity components are as follows.

$$u_i = \bar{u}_i + u'_i \tag{2-7}$$

Where $\bar{u}_i$ is the mean and u'_i is the fluctuating component of velocity [23].

Also for the scalar quantities like pressure, the same approach is applied.

$$\phi = \bar{\phi} + \phi' \tag{2-8}$$

In equation 2-18, ϕ represents a scalar such as pressure or energy [23].

Substituting this expression with the instantaneous continuity and momentum equations and taking the Reynolds-averaged Navier-Stokes approach leads to following equations.

$$\frac{\partial \rho}{\partial t} + \frac{\partial}{\partial x_i}(\rho u_i) = 0 \tag{2-9}$$

$$\frac{\partial}{\partial t}(\rho u_i) + \frac{\partial}{\partial x_j}(\rho u_i u_j) = -\frac{\partial p}{\partial x_i} + \frac{\partial}{\partial x_j}\left[\mu\left(\frac{\partial u_i}{\partial x_j} + \frac{\partial u_j}{\partial x_i} - \frac{2}{3}\delta_{ij}\frac{\partial u_l}{\partial x_l}\right)\right] + \frac{\partial}{\partial x_j}(-\rho\overline{u'_\iota u'_\jmath}) \tag{2-10}$$

Where in equation 2-10 each term of the equation are as follows.

- $\frac{\partial}{\partial t}(\rho u_i)$: Unsteady term
- $\frac{\partial}{\partial x_j}(\rho u_i u_j)$: Advection term
- $\frac{\partial p}{\partial x_i}$: Pressure gradient term

- $\frac{\partial}{\partial x_j}\left[\mu\left(\frac{\partial u_i}{\partial x_j}+\frac{\partial u_j}{\partial x_i}-\frac{2}{3}\delta_{ij}\frac{\partial u_l}{\partial x_l}\right)\right]$: Diffusion term

The term $(-\rho\overline{u'_\iota u'_j})$, known as the Reynolds shear stresses are related to the velocity gradient with a common approach known as the Boussinesq approximation as follow, where μ_t is the turbulent viscosity.

$$\rho\overline{u'_\iota u'_j}=\mu_t\left(\frac{\partial u_i}{\partial x_j}+\frac{\partial u_j}{\partial x_i}\right)-\frac{2}{3}\left(\rho k+\mu_t\frac{\partial u_k}{\partial x_k}\right)\delta_{ij} \tag{2-11}$$

for the $k-\varepsilon$ models two additional transport equation are solved including the turbulence kinetic energy (k) and turbulence dissipation rate (ε) to compute the turbulent viscosity as a function of k and ε.

2.2.1. Transport equations for the realizable $k-\varepsilon$ model

The general form of equations for realizable $k-\varepsilon$ model are described as follows.

$$\frac{\partial}{\partial t}(\rho k)+\frac{\partial}{\partial x_j}(\rho k u_j)=\frac{\partial}{\partial x_j}\left[\left(\mu+\frac{\mu_t}{\sigma_k}\right)\frac{\partial k}{\partial x_j}\right]+G_k+G_b-\rho\varepsilon-Y_M+S_k \tag{2-12}$$

$$\frac{\partial}{\partial t}(\rho\varepsilon)+\frac{\partial}{\partial x_j}(\rho\varepsilon u_j)=\frac{\partial}{\partial x_j}\left[\left(\mu+\frac{\mu_t}{\sigma_\varepsilon}\right)\frac{\partial\varepsilon}{\partial x_j}\right]+\rho C_1 S_\varepsilon-\rho C_2\frac{\varepsilon^2}{k+\sqrt{v\varepsilon}}+ \tag{2-13}$$

$$C_{1\varepsilon}\frac{\varepsilon}{k}C_{3\varepsilon}G_b+S_\varepsilon$$

Where $C_1=\max\left[0.43,\frac{\eta}{\eta+5}\right],\eta=S\frac{k}{\varepsilon},S=\sqrt{2S_{ij}S_{ij}}$ and G_k represents the turbulence kinetic energy generation from the mean velocity gradients and G_B is the turbulence kinetic energy generation due to buoyancy, while Y_M is the term for the contribution of fluctuating in dilatation in compressible turbulence to the overall dissipation rate, C_2 and $C_{1\varepsilon}$ are both constant. To close the equation, σ_k, σ_ε, S_k and S_ε are the turbulent Prandtl numbers and source terms for k and ε respectively. In above equations, $C_{1\varepsilon}=1.44$, $C_2=1.9$, $\sigma_k=1.0$ and $\sigma_\varepsilon=1.2$ [23].

In the realizable $k-\varepsilon$ model, like the standard and RNG $k-\varepsilon$ models, the turbulent viscosity is computed as follow, where $C_\mu = 0.09$ [23].

$$\mu_t = \rho C_\mu \frac{k^2}{\varepsilon} \tag{2-14}$$

The rest of the parameters from equations 2-12 and 2-13 are written as follow.

$$G_k = \mu_t S^2 \tag{2-15}$$

$$G_b = -g_i \frac{\mu_t}{\rho Pr_t} \frac{\partial \rho}{\partial x_i} \tag{2-16}$$

Effect of compressibility is also described by Y_M due to the high Mach number existing in the physics of process as follow, where M_t is the turbulent Mach number [23].

$$Y_M = 2\rho\varepsilon {M_t}^2 \tag{2-17}$$

$$M_t = \sqrt{\frac{k}{\gamma RT}} \tag{2-18}$$

2.2.2. Near wall treatment

The effect of solid walls on turbulence behaviour of the flow is significant; therefore, a precise prediction of the flow behavior near the wall can maintain the accuracy of the solution. Three different layers near the wall are shown in figure 2.1 [33].

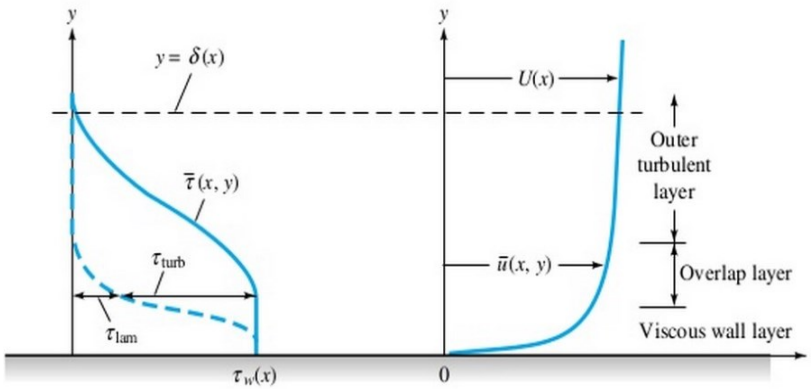

Figure 2.1 Velocity and shear distribution near the wall [33]

In viscous wall layer, molecular viscosity and viscous shear are dominant and the flow is almost laminar. Further away from the wall, turbulent shear becomes more important and the flow is changed to turbulence region. In between, there is a transitional layer in which both molecular and turbulent viscosities have significant effect [33].

2.2.3. Wall function

There are two different approaches for the near wall region. In the first approach, the viscous sublayer is solved all the way until it reaches the wall. In this approach, fine meshes are required near the wall; therefore, this method needs more computational time. In the second approach, semi empirical equations are utilized in order to connect the turbulent outer region to the wall region. This method is described as follow [23].

$$U^* = \frac{1}{k}\ln(Ey^*) \qquad y^* > 11.225 \tag{2-19}$$

$$U^* = y^* \qquad y^* < 11.225 \tag{2-20}$$

Where U^* is the dimensionless velocity and y^* is the dimensionless distance of the element from the wall and they can be calculated as follow [23].

$$U^* \equiv \frac{U_P C_\mu^{1/4} k_P^{1/2}}{\tau_w/\rho} \tag{2-21}$$

$$y^* \equiv \frac{\rho C_\mu^{1/4} k_P^{1/2} y_P}{\mu} \tag{2-22}$$

Where the parameters that are associated with these two terms are listed below.

- k = Von Karman constant (= 0.4187)
- E = Empirical constant (= 9.793)
- U_P = Mean velocity of the fluid at the wall-adjacent cell centroid
- k_P = Turbulent kinetic energy at the wall-adjacent cell centroid

- y_P = Distance from the centroid of the wall-adjacent cell centroid
- μ = Dynamic viscosity of the fluid

For highly compressible flows, the distribution of temperature near the wall is clearly different from subsonic flows, due to the viscous heating dissipation the law of wall for the temperature is as follows [23], [34].

$$T^* \equiv \frac{(T_w - T_P)\rho c_p C_\mu^{1/4} k_P^{1/2}}{\dot{q}} \tag{2-23}$$

$$T^* = Pry^* + \frac{1}{2}\rho Pr \frac{C_\mu^{1/4} k_P^{1/2}}{\dot{q}} U_P{}^2 \qquad y^* < y_t{}^* \tag{2-24}$$

$$T^* = Pr_t \left[\frac{1}{k}\ln(Ey^*) + P\right] + \frac{1}{2}\rho \frac{C_\mu^{1/4} k_P^{1/2}}{\dot{q}} \left\{Pr_t U_P{}^2 + (Pr - Pr_t)U_c{}^2 \right. \tag{2-25}$$

$$y^* > y_t{}^*$$

Where P is computed from the formula introduced as follow [23].

$$P = 9.24\left[\left(\frac{Pr}{Pr_t}\right)^{3/4} - 1\right]\left[1 + 0.28e^{-0.007Pr/Pr_t}\right] \tag{2-26}$$

From the equations 2-23 – 2-26, the utilized parameters for these equations are listed as follow.

- $\dot{q}$ = Wall heat flux
- c_P = Specific heat of the fluid
- k_P = Turbulent kinetic energy at the wall-adjacent cell centroid
- T_P = Temperature at the wall adjacent cell centroid
- T_w = Temperature at the wall
- Pr = Molecular Prandtl number
- Pr_t = Turbulent Prandtl number (0.85 at the wall)
- A = Van Driest constant (=26)

- U_c = Mean velocity magnitude at $y^* = y_t^*$

The effect of compressibility in equations 2-24 and 2-25 is considered according to the second terms of the right hand side of each equation [23].

2.3. Numerical technique

Governing equations in ANSYS-Fluent such as; momentum, mass, energy, etc. are solved based on finite volume method.

In this study, a pressure based solver (SIMPLE scheme) is chosen Solution loop for this segregated pressure-based algorithm is shown in Figure 2.2 [23]. For the sake of accuracy, the second order upwind scheme is used to solve the continuity, momentum and energy equations.

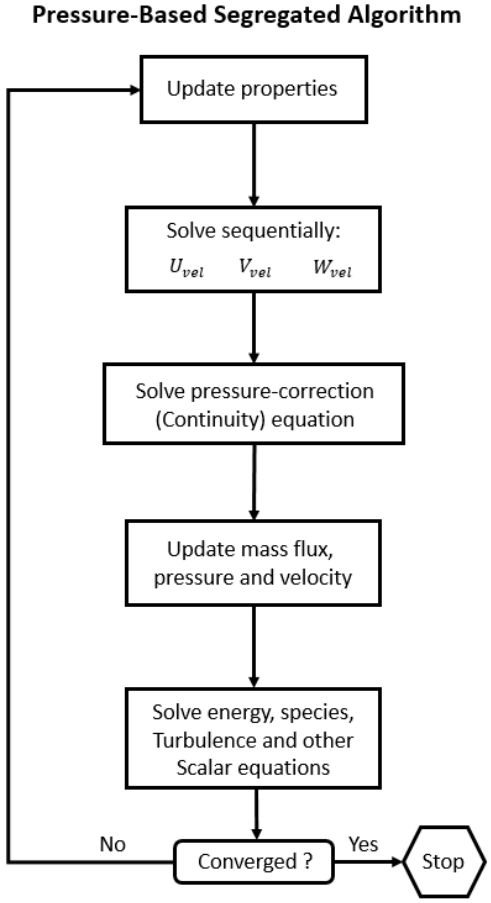

Figure 2.2 Solution algorithm for the pressure-based segregated solver [23]

2.4. Dispersed phase

After convergence of the solution for the continuous phase, a solution for dispersed phase is obtained by injecting particles into the calculated flow field that can exchange mass, momentum and energy with the continuous phase. Lagrangian particle tracking is used in this study to simulate the motion of the particles. Furthermore, particles are assumed to be solid, spherical and inert with negligible volume fraction. To predict the particles trajectory based on Lagrangian approach, main active forces applied to the particles should be taken into account as follow.

$$\frac{d\vec{u}_p}{dt} = F_D\left(\vec{u} - \vec{u}_p\right) + \frac{\vec{g}(\rho_P - \rho)}{\rho_P} + \vec{F} \qquad (2\text{-}27)$$

Where, the first term in the right hand side of the equation is the drag force per unit particle mass, the second term is the effect of gravitational force per unit particle mass and the third term is an additional acceleration force per unit particle mass. In above equation, F_D is calculated as follow.

$$F_D = \frac{18\mu}{\rho_p {d_p}^2}\frac{C_D Re}{24} \qquad (2\text{-}28)$$

The utilized parameters in equations 2-27 and 2-28 are listed as follow.

- $\vec{u}$ = Fluid phase velocity
- C_D = Drag coefficient
- $\vec{u}_p$ = Particle velocity
- μ = Molecular viscosity of the fluid
- ρ = Fluid density
- ρ_p = Particle density

- d_p = Particle diameter

The Reynolds number in these expressions are the particle Reynolds number calculated as follow.

$$Re = \frac{\rho d_p |\vec{u}_p - \vec{u}|}{\mu} \tag{2-29}$$

The gravitational force is neglected in this study due to the small particles mass and their negligible effect of the particles trajectory. For the additional force, effect of Thermophoretic force is studied in this work in presence of substrate. The reason behind this study is the existence of temperature gradient in this process when low temperature carrier gas reaches the ambient temperature at the bow shock location. At this point, it is expected to see the effect of Thermophoretic force in the opposite direction of temperature gradient. The equation of Thermophoretic force is as follow [23], [35], [36].

$$\vec{F} = -D_{T,p} \frac{1}{m_p T} \nabla T \tag{2-30}$$

Where, $D_{T,p}$ is the thermophoretic coefficient which is defined based on equation 2-30 suggested by Talbot [37].

$$D_{T,p} = \frac{6\pi d_p \mu^2 C_s (K + C_t Kn)}{\rho (1 + 3C_m Kn)(1 + 2K + 2C_t Kn)} \tag{2-31}$$

The utilized parameters in equations 2-30 and 2-31 are listed as follow.

- Kn = Knudsen number
- C_S = 1.17
- C_t = 2.18
- C_m = 1.14

- m_p = Particle mass
- T = Local fluid temperature

This expression is valid only for spherical particles and ideal gas assumption [23].

2.4.1. Drag coefficient

In this study, two drag expressions are compared with each other; where in the first drag expression, the effects of compressibility and rarefaction are neglected. The most widely used non-linear stokes drag correction in multiphase flow study is Schiller-Naumann drag expression, where in 2017, Johnson et al. used this expression in their study for particle tracking [16], [35]. The equation for this drag expression for Reynolds number less than 800 is as follow [38].

$$C_{D,Re} = f_{Re}\left(\frac{24}{Re_p}\right) \tag{2-32}$$

$$f_{Re} = 1 + 0.15{Re_p}^{0.687} \tag{2-33}$$

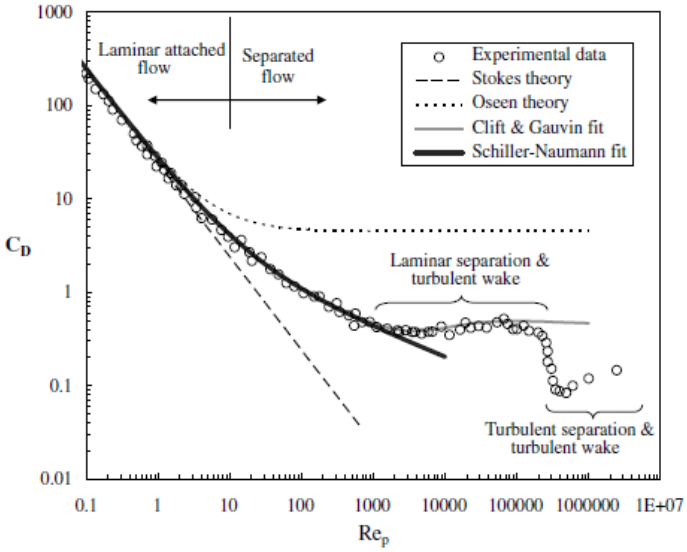

Figure 2.3 Drag coefficient for a smooth solid sphere at various Reynolds number for incompressible conditions with the reported experimental data [33]

To include the effect of compressibility and rarefaction, effect of Knudsen number and particles Mach number should be considered in the drag expression for the aerosol deposition spray simulation. Due to the low pressure inside the vacuum chamber, particles Knudsen number is greater than 1, therefore; the non-continuum condition exists in this process. Also due to the instant expansion of the gas inside the vacuum chamber, particle Mach numbers are much greater than 1; therefore, a drag expression defined based on the effect of compressibility and rarefaction of the carrier gas is necessary for simulation of a particles motion. Among different drag expressions for the compressible and rarefied condition such as; Crowe, Henderson and Hermsen; the most recent drag expression is introduced by Loth in 2008 that is suitable for hypersonic and vacuum conditions [39]. Figure 2.4 shows the deviation of this drag expression from the conventional expressions.

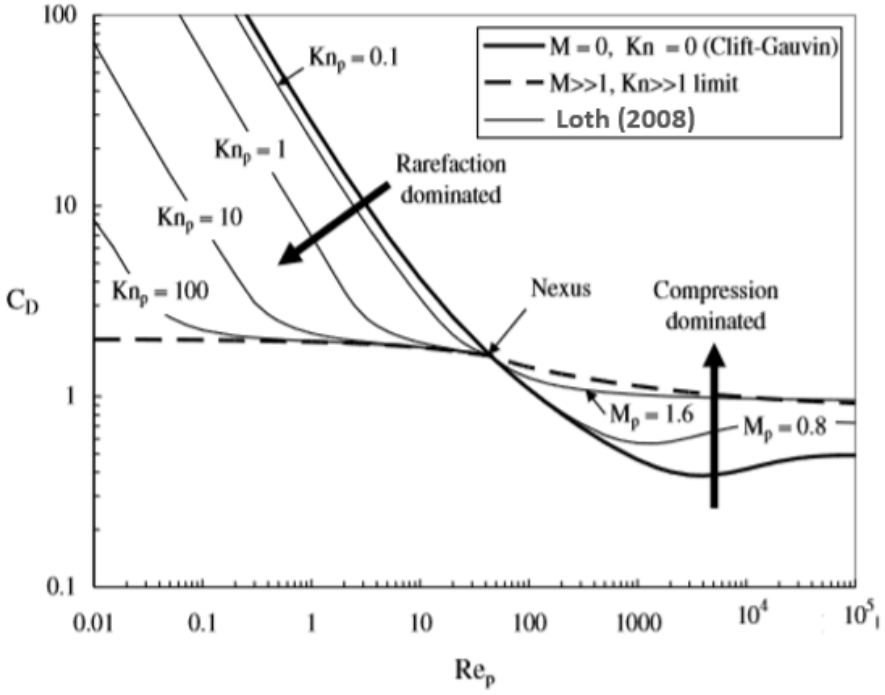

Figure 2.4 Rarefaction and compression effects on drag of spherical particles [39]

It can be concluded from figure 2.4 that, the incompressible drag expressions are only valid for continuum flow conditions in a certain range of Mach numbers. It can be also seen in figure 2.5 that the drag expression presented by Loth, is the most accurate expression compare with the other expressions.

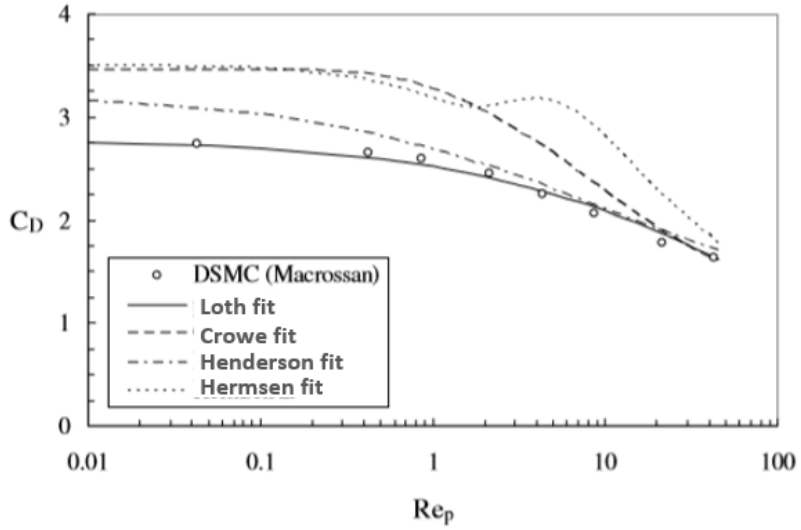

Figure 2.5 Different drag coefficient in $M_p = 2.95$ [39]

2.4.2. Compressibility and non-continuum parameters for drag

In order to consider the effects of compressibility and rarefaction on drag coefficient, the impact of these two parameters on the drag coefficient will become important. To clarify the level of compressibility, relative Mach number is introduced as follow [39].

$$M_p = \frac{|\vec{u}-\vec{u}_p|}{\sqrt{\gamma RT}} \tag{2-34}$$

Compressibility effect becomes significant when the relative Mach number is more than 0.4 that happens when particles are entrained with high speed carrier gas. In this case, particle's response time can lead to significant Mach number; therefore, compressibility effect becomes important for such conditions [39], [40].

To evaluate the validation of continuum condition, particle Knudsen number is defined as the ratio of mean free path of the surrounding gas molecules to the particle diameter. This expression, is also defined as follow based on particle's Reynolds and Mach number for the ideal gas law as follow proposed by Schaaf and Chambré [40].

$$Kn_p = \sqrt{\frac{\pi\gamma}{2}}\left(\frac{M_p}{Re_p}\right) \tag{2-35}$$

If the continuum condition is considered for $Kn_p \ll 1$, it can be concluded that, the continuum condition is violated in aerosol deposition process due to the low density condition (vacuum condition) and small particles diameter. Therefore, the consideration of rarefaction in drag force for the particles tracking is necessary [39].

In the suggested drag expression, the effect of Mach number, Knudsen number and Reynolds number are all considered due to the presence of different physical conditions existing during the spray process. This drag coefficient is expressed based on the relative Reynolds number and for $Re_p > 45$ is as follow for a compressible dominated flow [39].

$$C_M = \frac{5}{3} + \frac{2}{3}tanh\left[3\ln(M_p + 0.1)\right] \qquad \text{for } M_p \leq 1.45 \tag{2-36}$$

$$C_M = 2.044 + 0.2exp\left\{-1.8\left[\ln\left(\frac{M_p}{1.5}\right)\right]^2\right\} \qquad \text{for } M_p \geq 1.45 \tag{2-37}$$

$$G_M = 1 - 1.525{M_p}^4 \qquad \text{for } M_p < 0.89 \tag{2-38}$$

$$G_M = 0.0002 + 0.0008tanh\left[12.77(M_p - 2.02)\right] \quad \text{for } M_p > 0.89 \tag{2-39}$$

$$H_M = 1 - \frac{0.258C_M}{1+514G_M} \tag{2-40}$$

$$C_D = \frac{24}{Re_p}\left[1 + 0.15{Re_p}^{0.687}\right]H_M + \frac{0.42C_M}{1+\frac{42500G_M}{{Re_p}^{1.16}}} \qquad \text{for } Re_p > 45 \tag{2-41}$$

When $Re_p < 45$, the rarefaction effect is become dominant; therefore, the effect of particles Knudsen number should be taken into account. In such conditions, the drag coefficient is as follow [39].

$$f_{Kn} = \frac{1}{1+Kn_p[2.514+0.8\exp\left(\frac{-0.55}{Kn_p}\right)} \tag{2-42}$$

This empirical equation is introduced to add Knudsen number and the slip effect in Schiller-Naumann expression as follow [39], [41].

$$C_{D,Kn,Re} = C_{D,Re} f_{Kn} = \frac{24}{Re_p}\left(1 + 0.15{Re_p}^{0.687}\right) f_{Kn} \tag{2-43}$$

This expression is appropriate for free-molecular flow, in which the drag is no longer proportional to the viscosity. Moreover, Mach number is considered small in this expression and to extend this expression for high Mach number condition, another term called molecular speed ratio is introduced as follow [39].

$$s = M_p\sqrt{\frac{\gamma}{2}} \tag{2-44}$$

$$C_{D,fm} = \frac{(1+s^2)exp(-s^2)}{s^3\sqrt{\pi}} + \frac{(4s^4+4s^2-1)\mathrm{erf}(s)}{2s^4} + \frac{2}{3s}\sqrt{\pi\frac{T_p}{T_\infty}} \tag{2-45}$$

In equation 2-51, the first two terms of the right hand side refer to diffuse reflection; while the third term refers to particle temperature ratio. In this expression, T_∞ is the surrounding gas temperature whereas, T_p is the particle temperature. This equation is valid for non-thermal equilibrium conditions that happens in most of spray technologies that, particles are undergoing rapid heating or cooling due to the injection conditions or shock interactions. In case of thermal equilibrium where $T_p = T_\infty$, equation 2-51 is equal to the Epstein [42] model and can be written as follow.

$$C'_{D,fm} = \frac{(1+s^2)exp(-s^2)}{s^3\sqrt{\pi}} + \frac{(4s^4+4s^2-1)\mathrm{erf}(s)}{2s^4} \quad (2\text{-}46)$$

From the equations 2-45 and 2-46, the empirical drag expression for finite Reynolds number for free-molecular flow is as follow [39].

$$C_{D,fm,Re} = \frac{C_{D,fm}}{1+\left(\frac{C'_{D,fm}}{1.63}-1\right)\sqrt{\frac{Re_p}{45}}} \quad (2\text{-}47)$$

Following expression is appropriate for hypersonic conditions whereas, $s \geq 1$ and become undefined when Mach number gets zero value; therefore, following empirical expression is proposed for the overall drag coefficient with finite Reynolds number [39].

$$C_D = \frac{C_{D,Kn,Re}}{1+{M_p}^4} + \frac{{M_p}^4 C_{D,fm,Re}}{1+{M_p}^4} \qquad for\ Re_p \leq 45 \quad (2\text{-}48)$$

2.5. Geometry and boundary conditions

The simulated spray nozzle, is a slit nozzle with the exit dimensions of $0.4 \times 10\ mm^2$ utilized by Naoe et al. [14] which the 3D view of nozzle's geometry is presented in figure 2.6 and half of the nozzle's cross section in front plane is given in figure 2.7 along the axis.

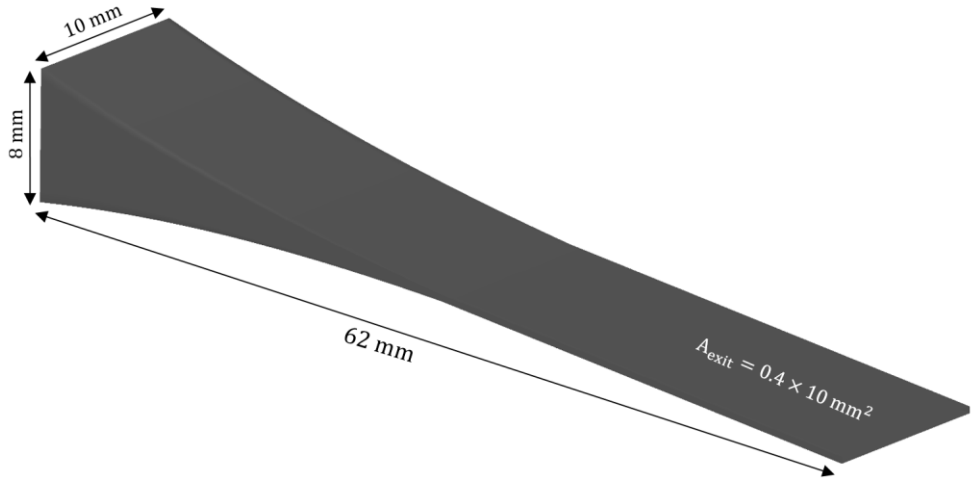

Figure 2.6 3D geometry of the nozzle

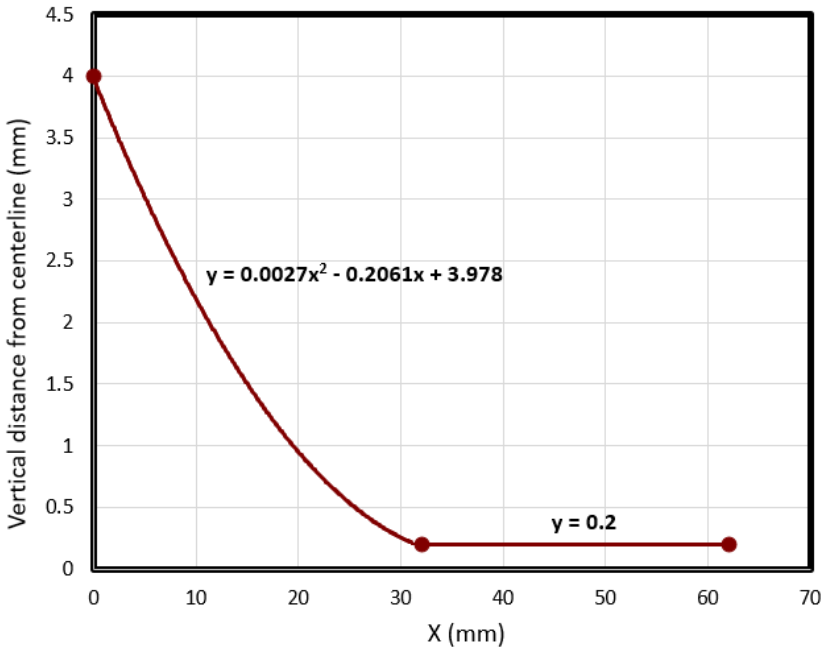

Figure 2.7 Cross section of the geometry along centerline

In this work, Nitrogen is utilized as a carrier gas to study the effect of carrier gas flow rate in free-jet case and the effect of substrate including bow shock, particle deceleration and standoff distance in the aerosol deposition process. These conditions are described as follow in table 2.3 for the simulation.

Flow rate (Free-Jet)	Standoff distance (Flow rate = 5 L/min)
2.5 L/min	4 mm
5.0 L/min	8 mm
7.5 L/min	16 mm

Table 2.1 Modeling conditions for free-jet and with the presence of the substrate

For the boundary conditions, the mass flux is utilized for the inlet boundary condition and for the outlet the pressure inside the vacuum chamber is given to the solver which is set to the constant value of 150 Pa used by Naoe et al. [13]. The stagnation temperature in this study is also 300 K and the boundary condition for the wall of the nozzle is the isothermal with the no slip boundary condition.

For the dispersed phase, the fine alumina particles are injected from the nozzle inlet based on the size distribution utilized by Naoe et al. [13]. To implement this distribution for the simulation, the expression of distribution is transferred to the Rosin-Rammler cumulative distribution (Mugele and Evans, 1951) available in ANSYS Fluent 14.5, where equation 2.49 describes this expression [23], [35].

$$F_m(D) = 1 - \exp\left[\left(\frac{D}{\delta}\right)^n\right] \tag{2-49}$$

The exact cumulative distribution and the approximated one using Rosin-Rammler distribution is shown in figure 2.8 based on the obtained values for the utilized parameters.

Where, $F_m(D)$ is the mass fraction smaller than a given diameter (D), $\delta = 3.3\ \mu m$ is the mean diameter and $n = 2.75$ is the Rosin-Rammler exponent. The particle mass flow rates are assumed to be 0.25, 0.5 and 0.75 g/min for carrier gas flow rates of 2.5, 5 and 7.5 L/min,

respectively. It is also assumed that, the particles are entering the domain from the inlet surface with the carrier gas. The boundary conditions for the walls inside the nozzle is assumed to be reflect which means that, once a particle hit the surface it bounces off with the same angle. For the substrate surface the boundary condition is assumed to be trapped, since it is assumed that the particle adheres to the substrate.

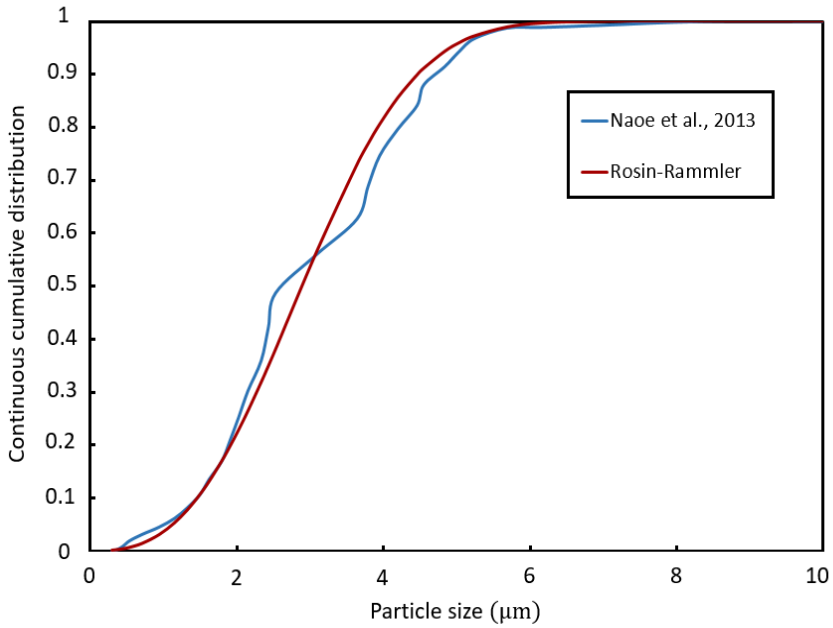

Figure 2.8 Cumulative particle size distribution using the exact distribution and Rosin-Rammler

2.6. Mesh and computational domain

The numerical analysis is done based on the nozzle geometry mentioned above working with a compressed Nitrogen gas discharging in a vacuum chamber; therefore, the computational domain includes the nozzle and the area around the exit of the nozzle inside the vacuum chamber for free-jet CFD analysis. In order to study the effect of standoff distance, a flat rectangular substrate with the cross sectional area of $5 \times 3\ cm^2$ and $2\ mm$ thickness is placed in different standoff distances.

These two geometries including their meshes and boundary conditions are shown in Figures 2.9 and 2.10 as follows, where only one quarter of the physical domain is simulated in terms of computational cost efficiency. The XY and XZ planes are set as symmetry boundaries. In this study, total number of cells are set to 2,200,000 cells for the free-jet simulation and for the standoff distance study, number of cells inside the domain before the substrate are as same as the number of cells in free-jet domain before the certain location of the substrate.

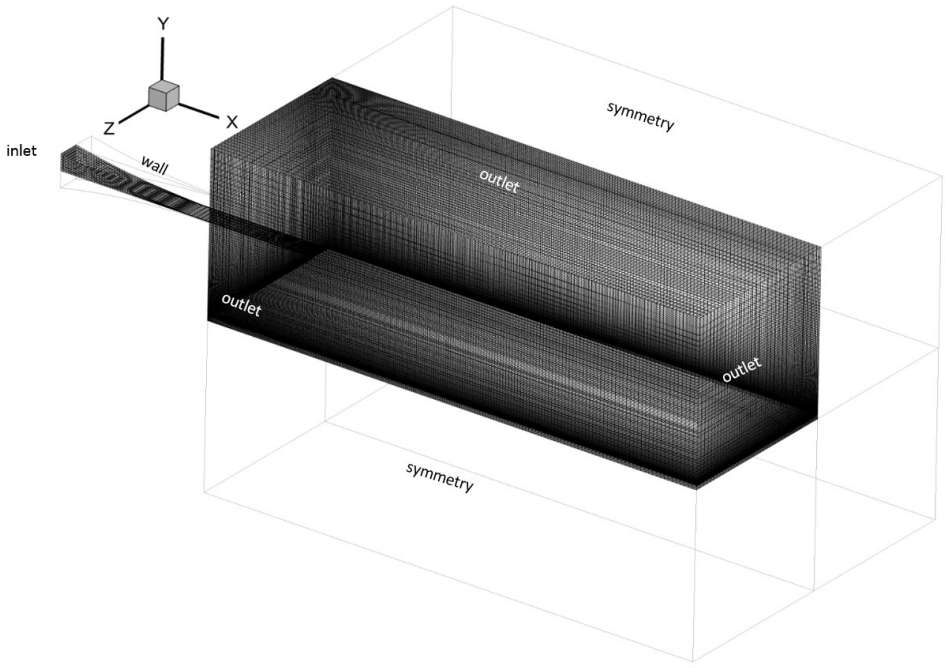

Figure 2.9 Computational domain and mesh for free jet simulation

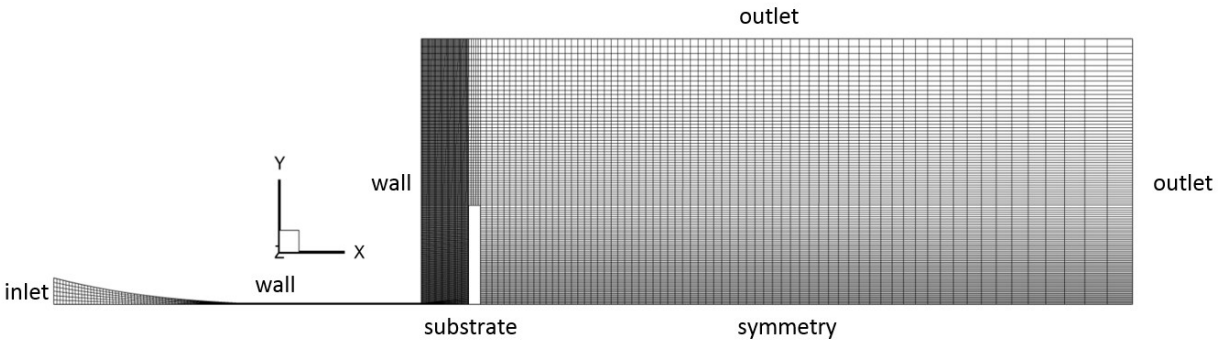

Figure 2.10 Computational domain and mesh for substrate effect analysis

3. Results

Overview

In this chapter, numerical results for continuous and dispersed phases are presented including the theoretical and experimental validations. Moreover, numerous factors such as drag expression, and effect of three dimensional analyses are discussed. At the end, the impact of gas flow rate and standoff distance on inflight particles characteristics are studied.

3.1. Validation

In this section, the numerical results from a 2D axisymmetric study case for the gas flow are validated based on the theoretical and experimental study of highly under-expanded flow by Crist et al. [24] and for the particle phase the numerical results are validated for the 2D planar slit nozzle with the PIV results measured by Naoe et al. [13].

3.1.1. Continuous phase

According to the geometry of the nozzle, a 2D axisymmetric computational domain is created for this study as shown in figure 3.1; while the boundary conditions and nozzle geometry are all set based on the operating conditions and experimental setup presented by Crist et al. [24]. In this study, a circular converging nozzle with 13 mm length and exit diameter of 2.25 mm is utilized with nitrogen gas in 300 K to validate the numerical approach with the theory and experiment.

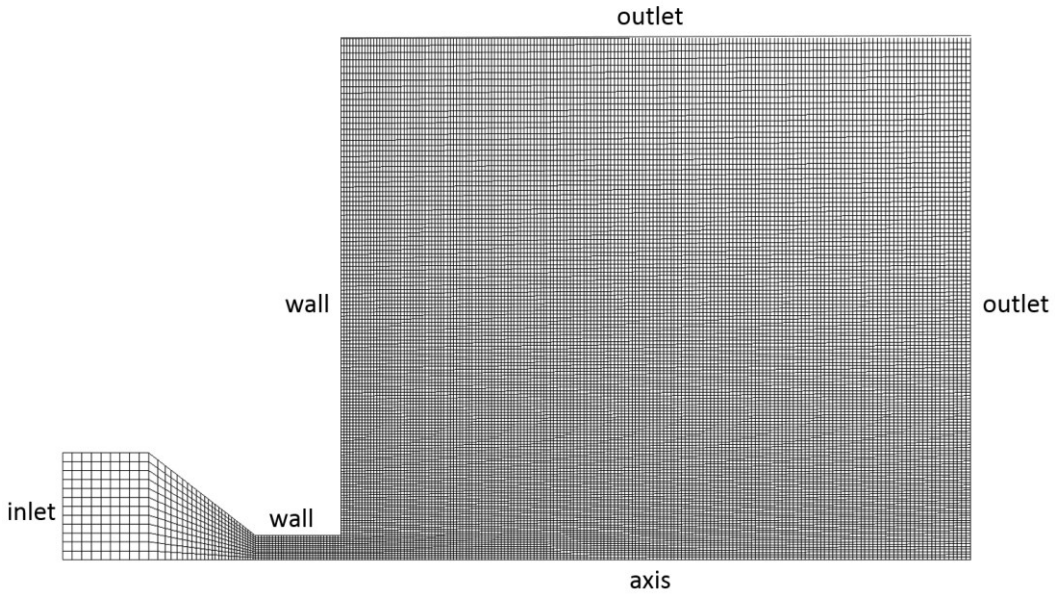

Figure 3.1 Computational domain including circular converging nozzle and a vacuum chamber

For the inlet boundary, three different flow rates of 3, 6 and 13 L/min are utilized in this study with the constant back pressure of 150 Pa inside the vacuum chamber.

In order to validate the solver for the continuous phase, the contours and plots of velocity magnitude and the Mach number are presented for three different gas flow rates to compare the numerical results with the theory and experimental data.

According to the figures 3.2 and 3.3, the gas is accelerated due to the pressure gradient between the inlet region and the outlet and after releasing inside the vacuum chamber a significant normal shock happens because the pressure at the exit of the nozzle is much lower than the pressure inside the vacuum chamber leading to a significant expansion during the spray. The Mach number associated with the 13 L/min flow rate is the highest compare with two other flow rates which is also the result of higher pressure ratio and more significant expansion during the spray process.

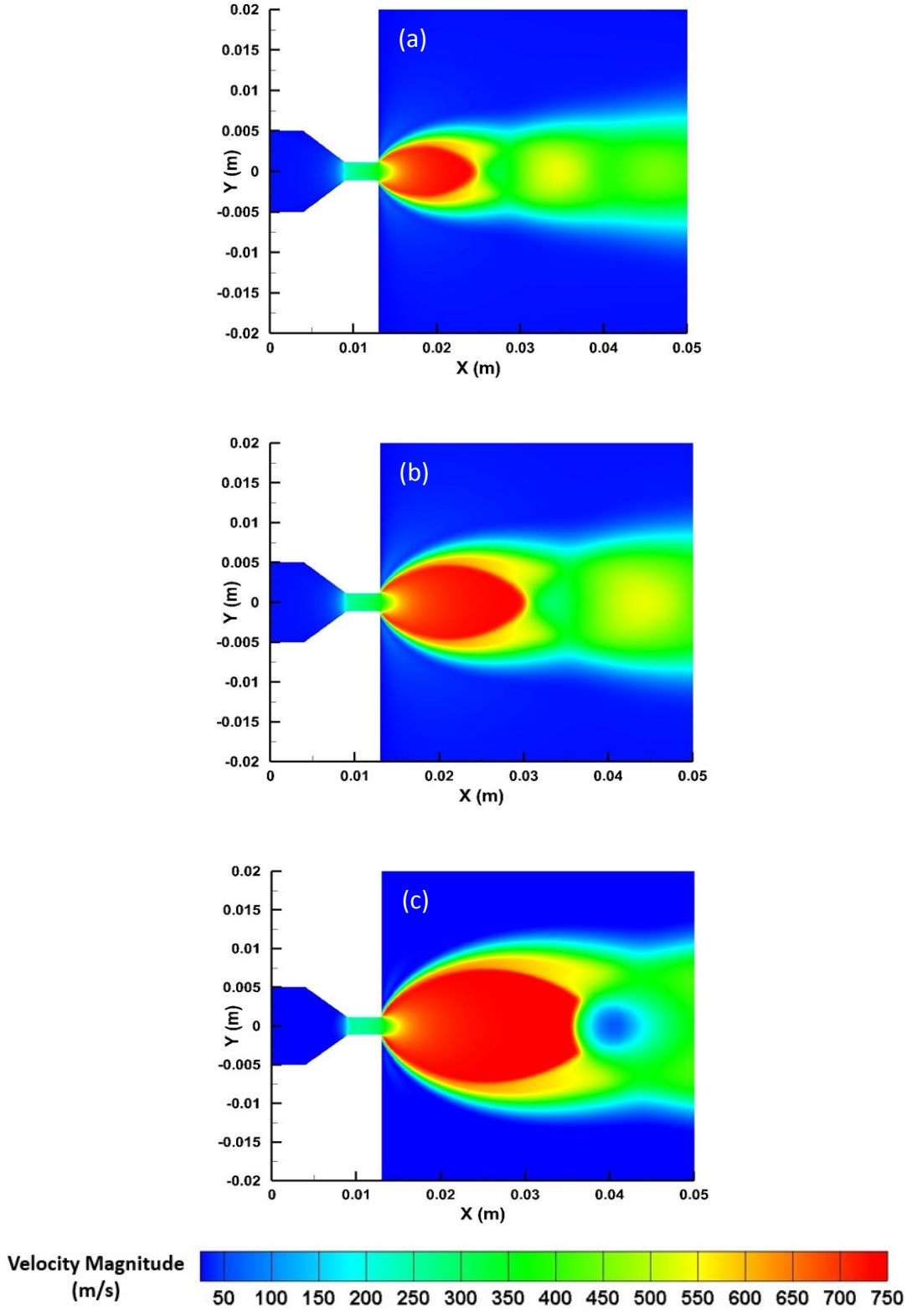

Figure 3.2 Contours of velocity magnitude for different flow rates a) 3, b) 6 and c) 13 L/min

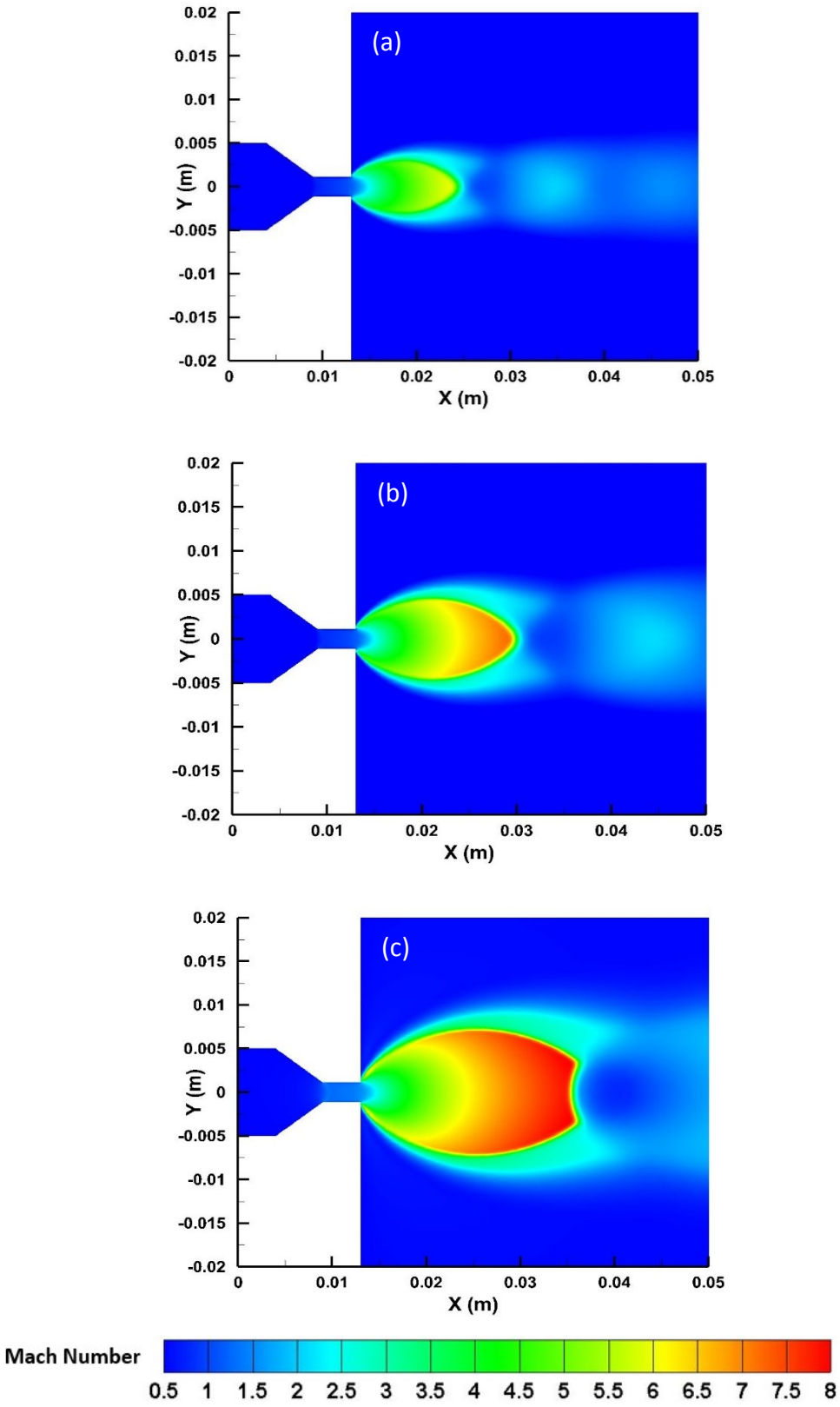

Figure 3.3 Contours of Mach number for different flow rates a) 3, b) 6 and c) 13 L/min

The Mach number contours for different flow rates shows that the Mach disk becomes larger for higher flow rates due to higher pressure ratio; moreover, the Mach disk location is shifted outward from the nozzle exit by increasing the flow rate.

In order to present the effect of flow rate on the Mach disk location, Mach number is plotted for different flow rates along the centerline of the nozzle in figure 3.4 where the indicated points of A, B and C in the graph represent the location of the Mach disk and the Mach number upstream of the shock. Furthermore, in Table 3.1, the numerical results are also compared with the experimental and theoretical results from Crist et al. [24].

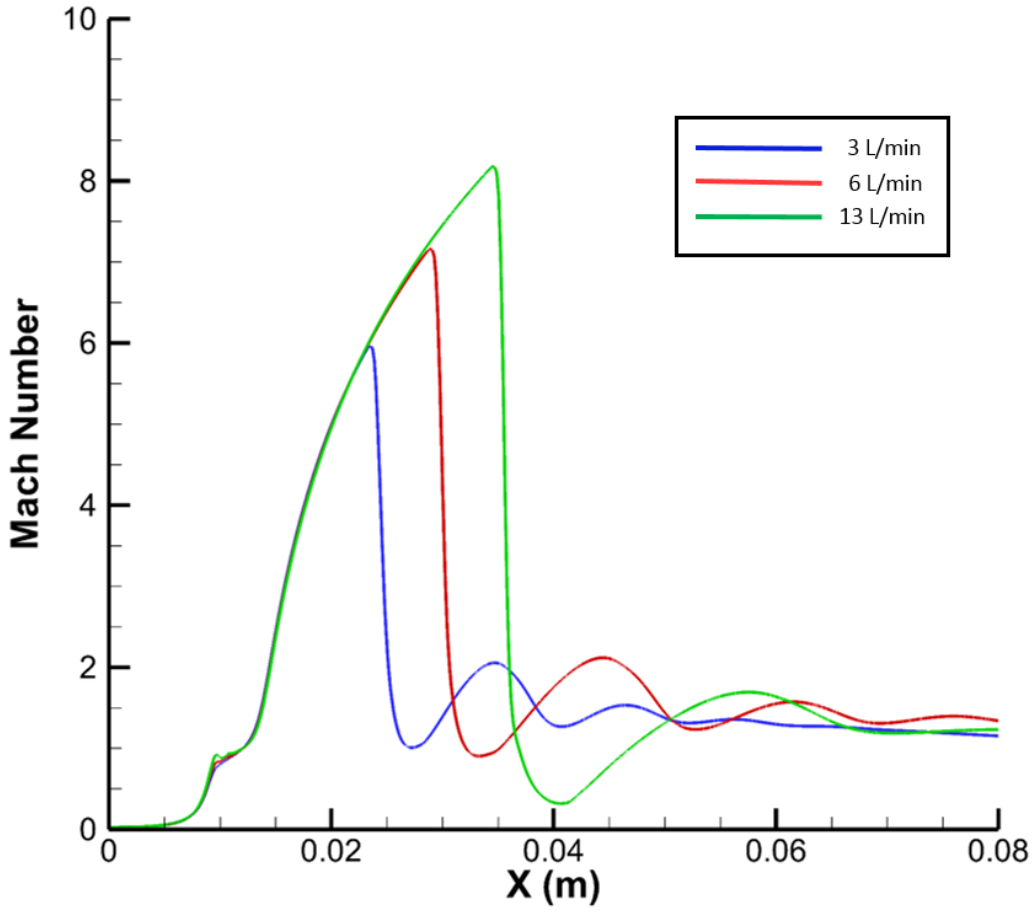

Figure 3.4 Mach number along the centerline

Flow rate	$3\ L/min$	$6\ L/min$	$13\ L/min$
$X_m(Exp)$	10.3 mm	15.8 mm	20.9 mm
$X_m(Num)$	10.4 mm	16.1 mm	21.4 mm
$M_{max}(Exp)$	6.2	7.5	8.4
$M_{max}(Num)$	6	7.2	8.2

Table 3.1 Mach disk location and Mach number upstream of the shock for different flow rates

According to table 3.1, the obtained values for Mach disk location and the Mach number upstream of the shock from the numerical simulation are close to experimental values; therefore, the selected numerical approach is suitable for continuous phase modeling.

3.1.2. Dispersed phase

In order to predict the inflight particles velocity, the solution for dispersed phase is validated based on the measured velocity of particles with PIV method. The measurement is done by Naoe et al. for alumina particles at 8mm distance from nozzle exit [13]. Here, a 2D planar model is created to model the spray nozzle and the vacuum chamber in order to just show the effect of compressibility and rarefaction on inflight particles velocity. Therefore, two drag expressions are utilized where the first one is suitable for hypersonic flows considering both compressibility and rarefaction presented by Loth in 2008 [39] and the other one is the Schiller-Naumann drag expression widely used for spray applications not considering the compressibility and rarefaction effects [38]. The gravity force and also the additional force term for the applied force equation is also neglected in this study and the only effective force is the drag force applied to the particles.

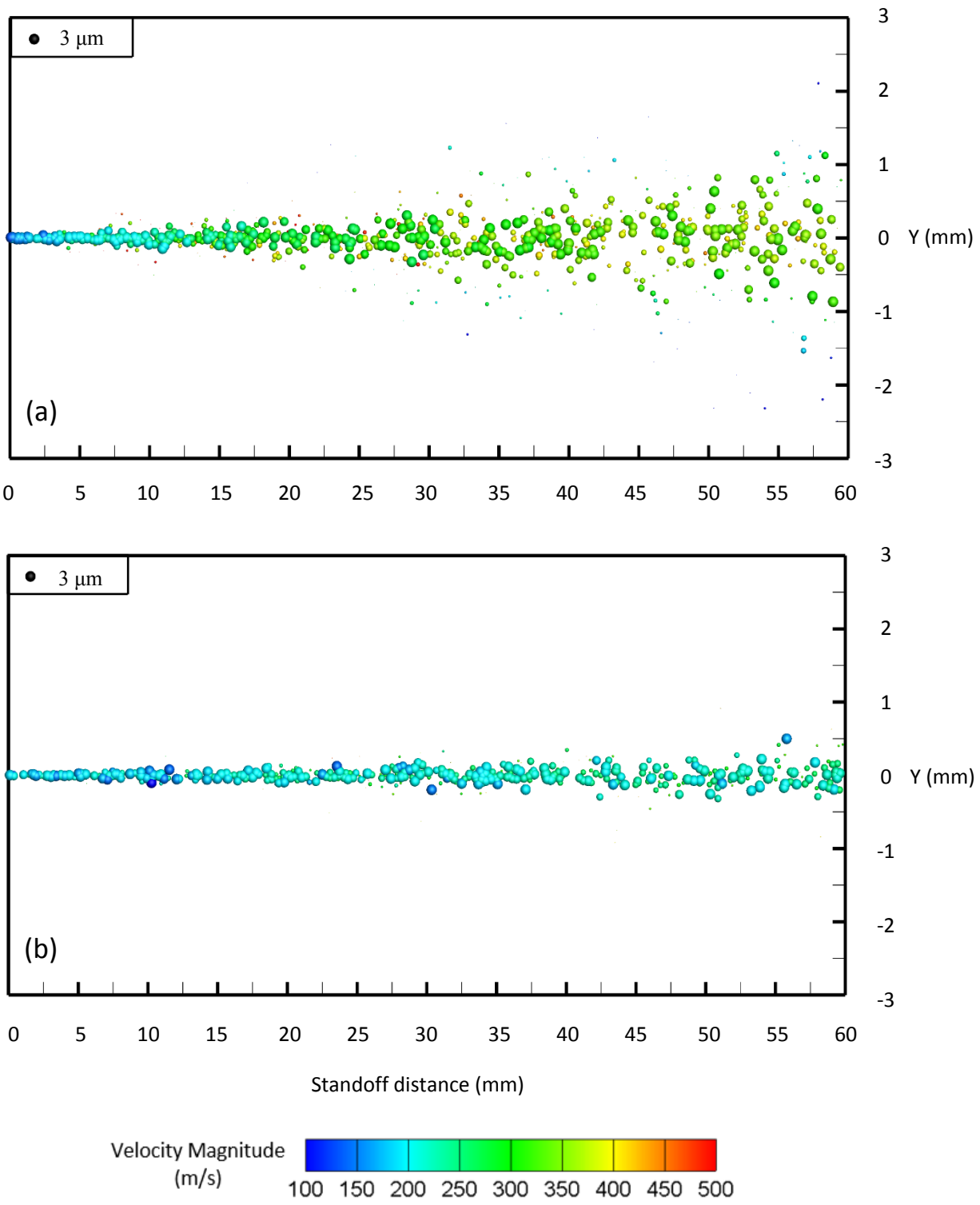

Figure 3.5 Particle velocity magnitude with two different drag models
a) Schiller-Naumann and b) Loth

The particles velocity is shown in figure 3.5 for different drag expressions with 5 L/min gas flow rate where, 3.5 (a) represents the particle tracking without consideration of compressibility and rarefaction in drag force while, 3.5 (b) is obtained by implementing the effect of Mach number and Knudsen number for the calculation of drag coefficient. It can be concluded that, not only the particle velocity but also the spray angle is affected by changing the drag coefficient. It can be inferred from figure 3.5 that, neglecting the effect of compressibility and rarefaction leads to higher velocity prediction for the particles. In order to compare the predicted particles velocity with the experimental data from Naoe et al. [13], particles velocity distribution at 8 mm distance from the nozzle exit is plotted for both drag formulas in figure 3.6 in order to show the effect of compressibility and rarefaction for particle velocity prediction.

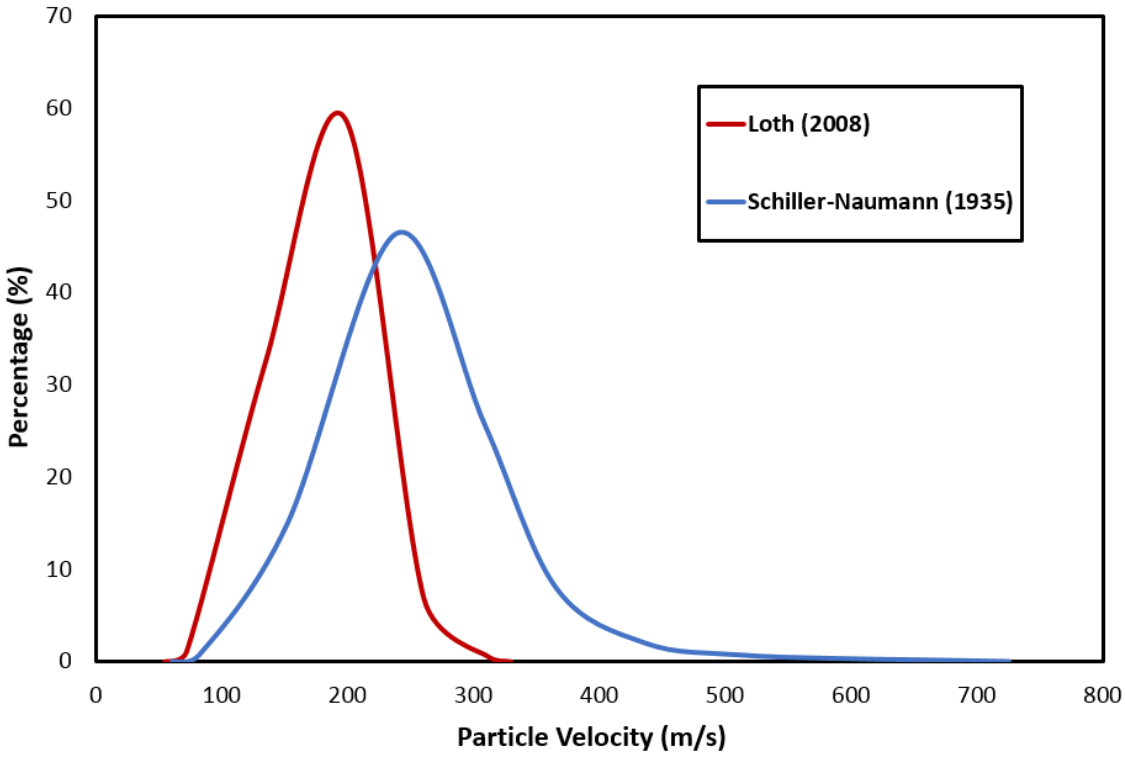

Figure 3.6 Particles velocity distribution using two drag models

To compare the obtained data from these two different approaches, the predicted velocities including the maximum, minimum and mean velocity for both cases are presented in table 3.2 and the mean velocity obtained from each drag model is compared with the experimental value.

Velocity / Drag	Maximum	Minimum	Average	Standard deviation	Error (%)
Loth	342 m/s	67 m/s	190 m/s	87	5
Schiller-Naumann	725 m/s	77 m/s	263 m/s	206	30
Particles average velocity measured with PIV method by Naoe et al. [6] = 200.3 m/s					

Table 3.2 Particle velocity distribution data at 8 mm distance from nozzle exit

3.2. Gas flow modeling

3.2.1. Mesh dependency test

In order to examine the dependency of the results to the grid size, a grid refinement test has been carried out in this section. This study is only implemented for continuous phase without the presence of the substrate for one quarter of the 3D model. Three levels of grid size are chosen for this study, a coarse grid with a total of 800,000 elements, a fine grid with a total of 2,200,000 elements and an ultra-fine grid with a total of 4,600,000 elements where, the number of nodes in each coordinates is roughly doubled from one size to the other one. The mesh dependency of the solution for this study is examined for velocity magnitude and Mach number along the centerline in figure 3.7 (a)-(b) to show the accuracy of the results. It can be inferred from these two plots that the solution obtained from the fine grid size with 2,200,000 elements and ultra-

fine grid size with 4,600,000 elements are almost identical and the largest difference between the solution of these two grids are less than 4 % at worst; therefore, the fine grid size mesh with the total of 2,200,000 elements are utilized in this study to consider both accuracy and also computational costs. In this mesh dependency test, all the residuals were below 10^{-6}.

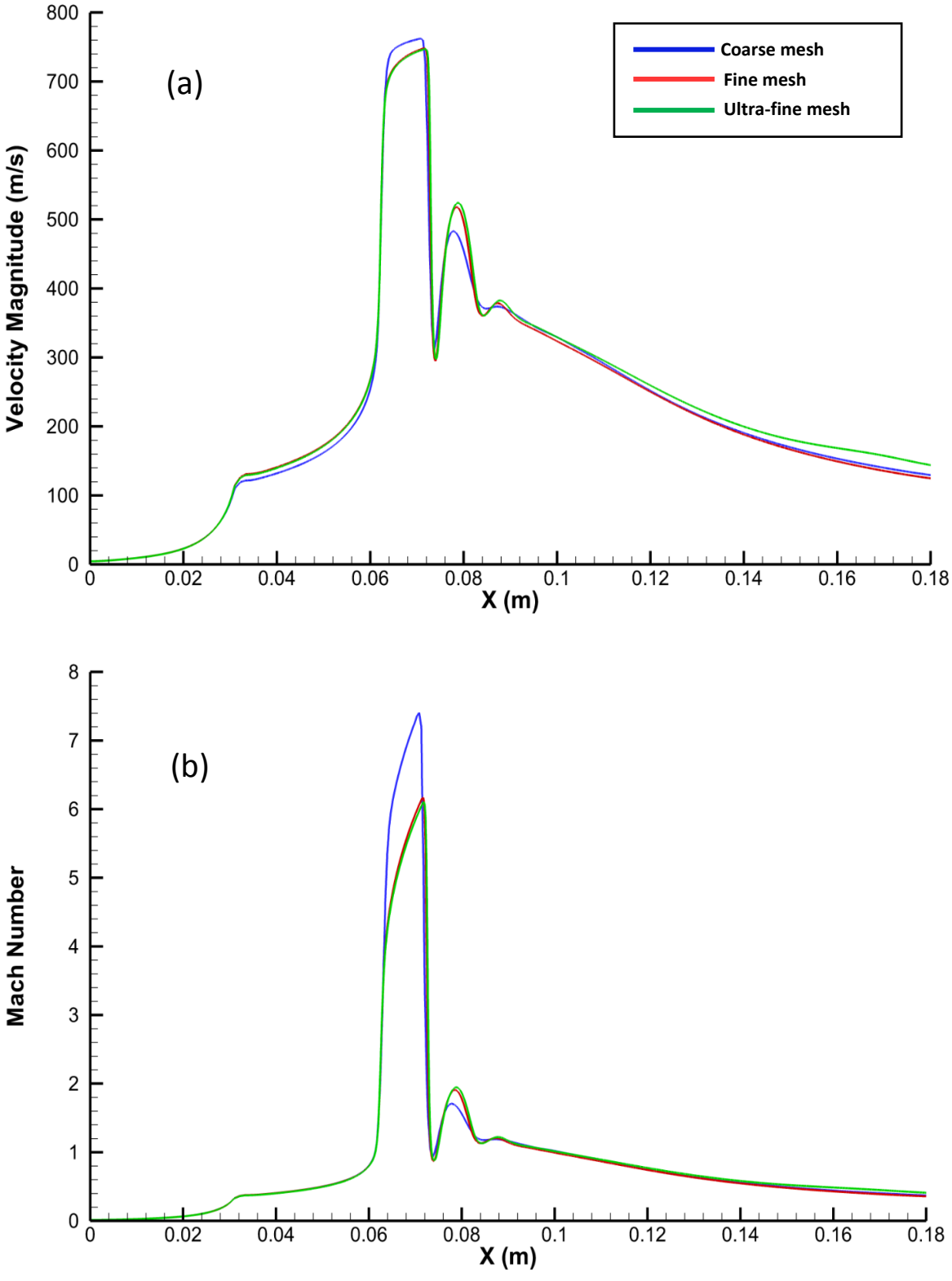

Figure 3.7 Velocity magnitude and Mach number along the centerline with different grid size

3.2.2. Comparison between 2D and 3D models

In order to simulate the gas flow, two different approaches are utilized based on the computational domain associated with the physical system. The first one is the 2D planar approach which the depth of the slit is considered very long compare the width of it. The second approach is a 3D quarter slice of the physical domain. The motivation of this study is to compare the effect of 3D analysis on velocity and Mach number profiles, because these two parameters can affect in-flight particles velocity and trajectory leading to different prediction for particles behavior during the spraying. This effect is shown in figures 3.8 and 3.9 for velocity magnitude and Mach number for the free jet with 5 L/min gas flow rate.

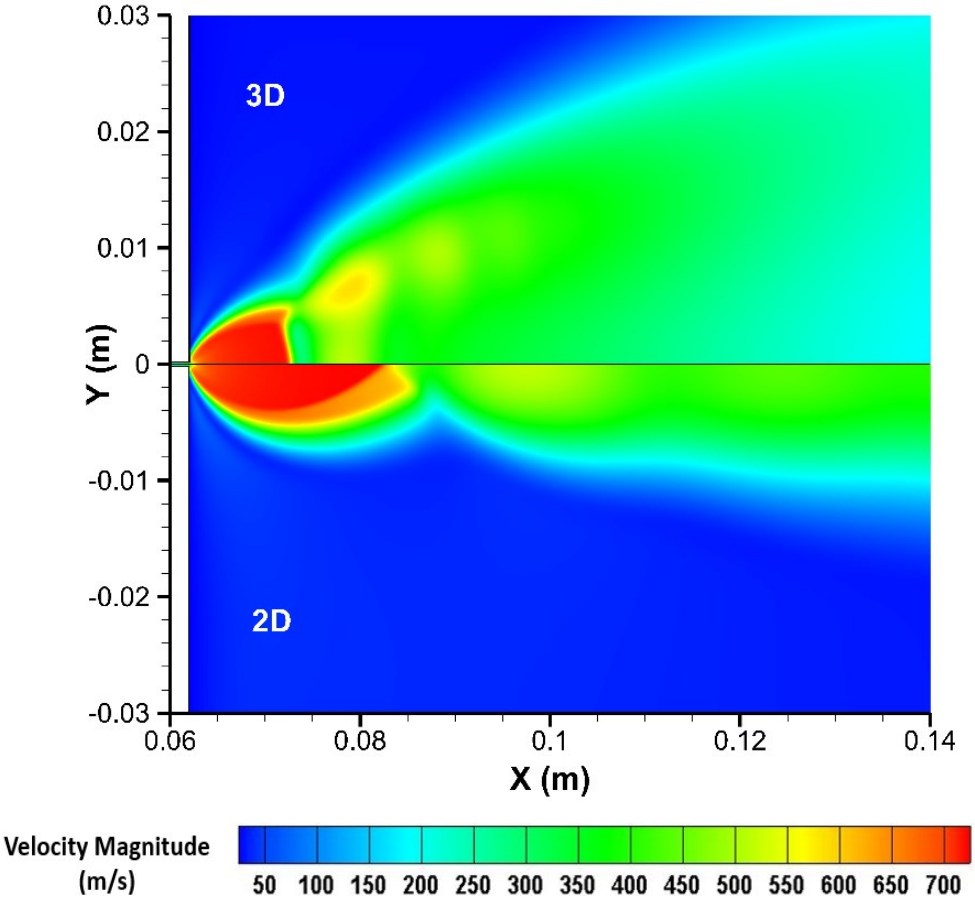

Figure 3.8 Velocity magnitude for both 2D planar and 3D models

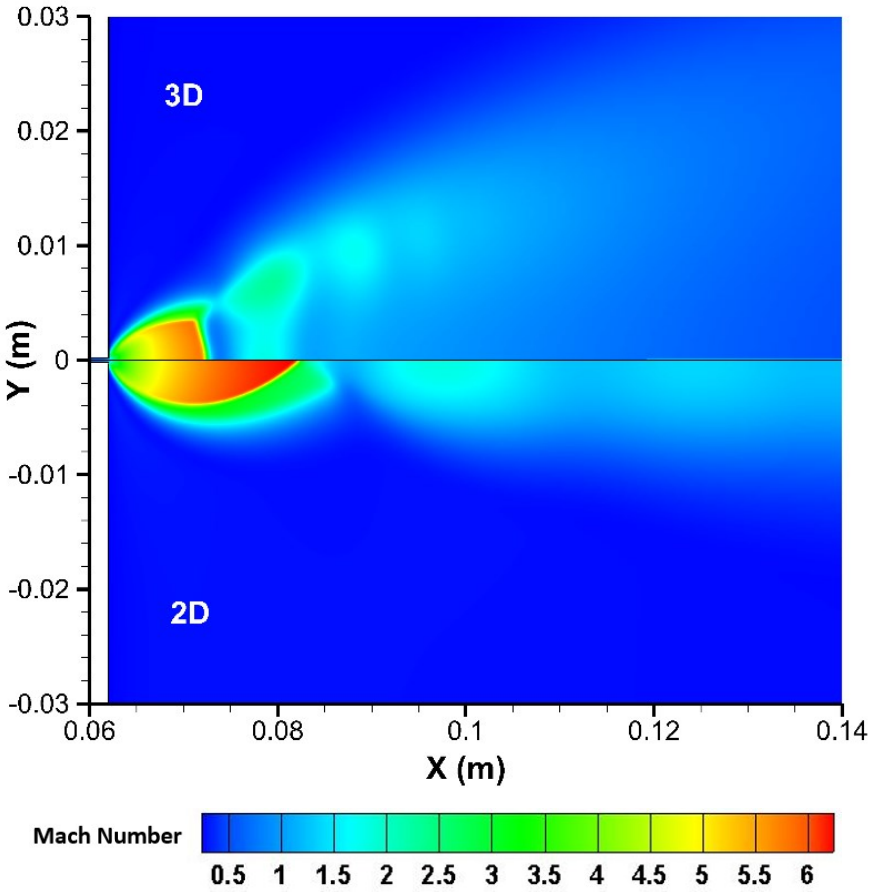

Figure 3.9 Mach number profile for both 2D and 3D models

It can be concluded from the velocity magnitude and Mach number contours that, using 2D planar model eliminates the Mach disk and significantly changes the formation of the shocks in certain locations. In this model, the simulated results are almost identical before the $X = 0.07\ m$ where the Mach disk is located. This normal shock can change particles trajectory; therefore, it is expected to see difference between the predicted particles trajectory from 2D to 3D analysis after this location.

Since most of the particles are moving with the carrier gas around the centerline of the nozzle, these two parameters are plotted along the centerline of the nozzle.

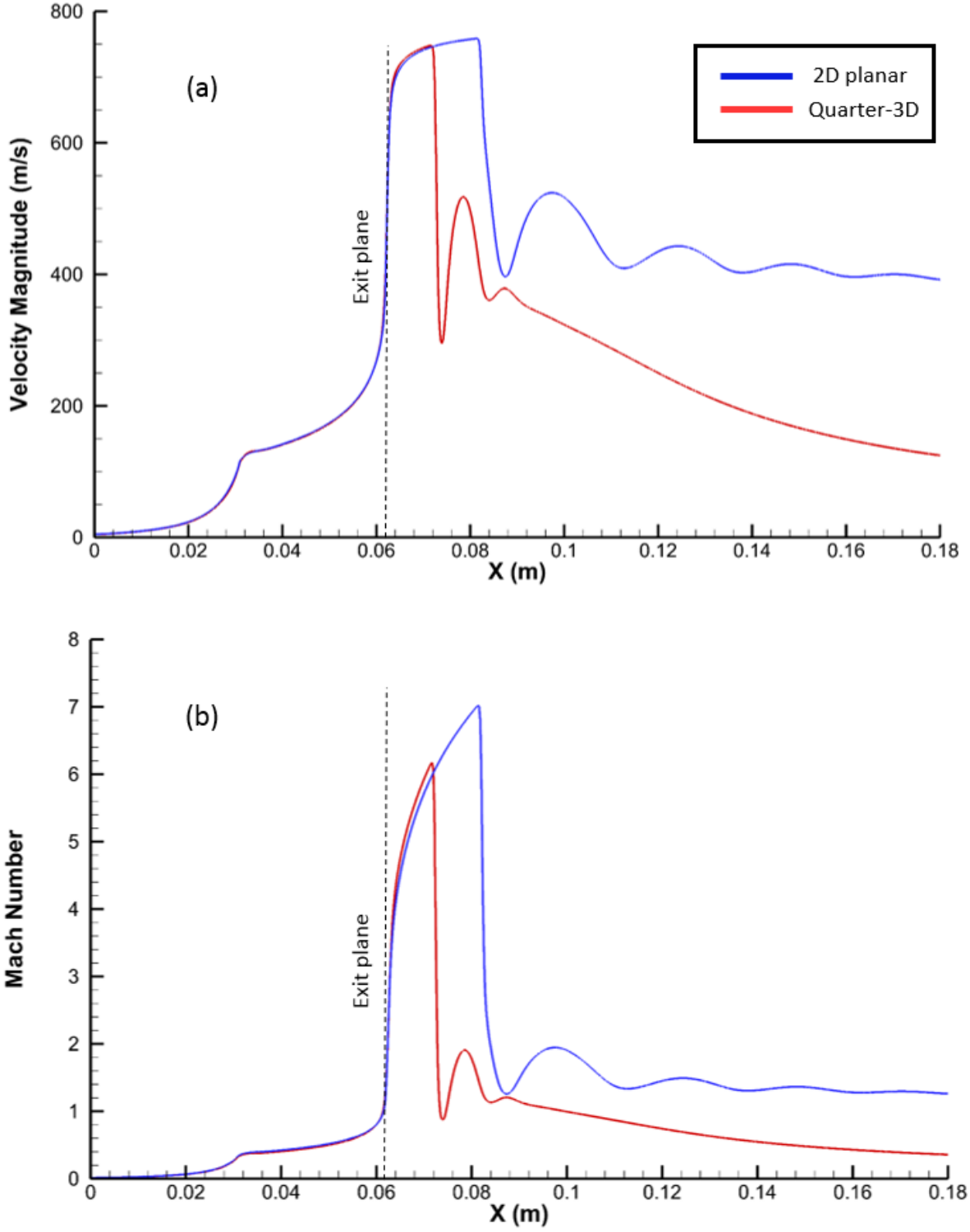

Figure 3.10 Plot of velocity magnitude and Mach number for 2D and 3D models along centerline

It can be inferred from these plots that particles velocity and trajectory prediction in 2D analysis is valid only before the Mach disk location. Where in this study, the 2D analysis will be reliable only until 10 mm distance from the exit of the nozzle.

In order to show the non-symmetric behavior of the jet, an iso-surface of velocity magnitude with the velocity contour at different standoff distances (SD) from the exit of the nozzle are shown in Figure 3.11 for the 3D model. It can be inferred from the mentioned figure, the "axis-switching" and "bifurcation" phenomena happen for this non-circular jet. When the gas exits the nozzle, the cross sectional area of the jet is close to the cross section of the nozzle's exit, but after the expansion of the jet, it gradually tends to increase its diameter along the minor axis, where eventually leading to a situation that the diameter of the jet is larger along the minor axis of the nozzle compare with its major axis. The continuous increase of the jet diameter along the minor axis of the nozzle with the continuous decrease of its diameter along the major axis of the nozzle will result in separation of the jet into two portions as it shown in Figure 3.10 known as bifurcation. This phenomenon can be important since the in-flight particle velocities and trajectories can be affected by the gas flow field. Axis-switching can change the location of the shocks and as a result it can affect the particle trajectories.

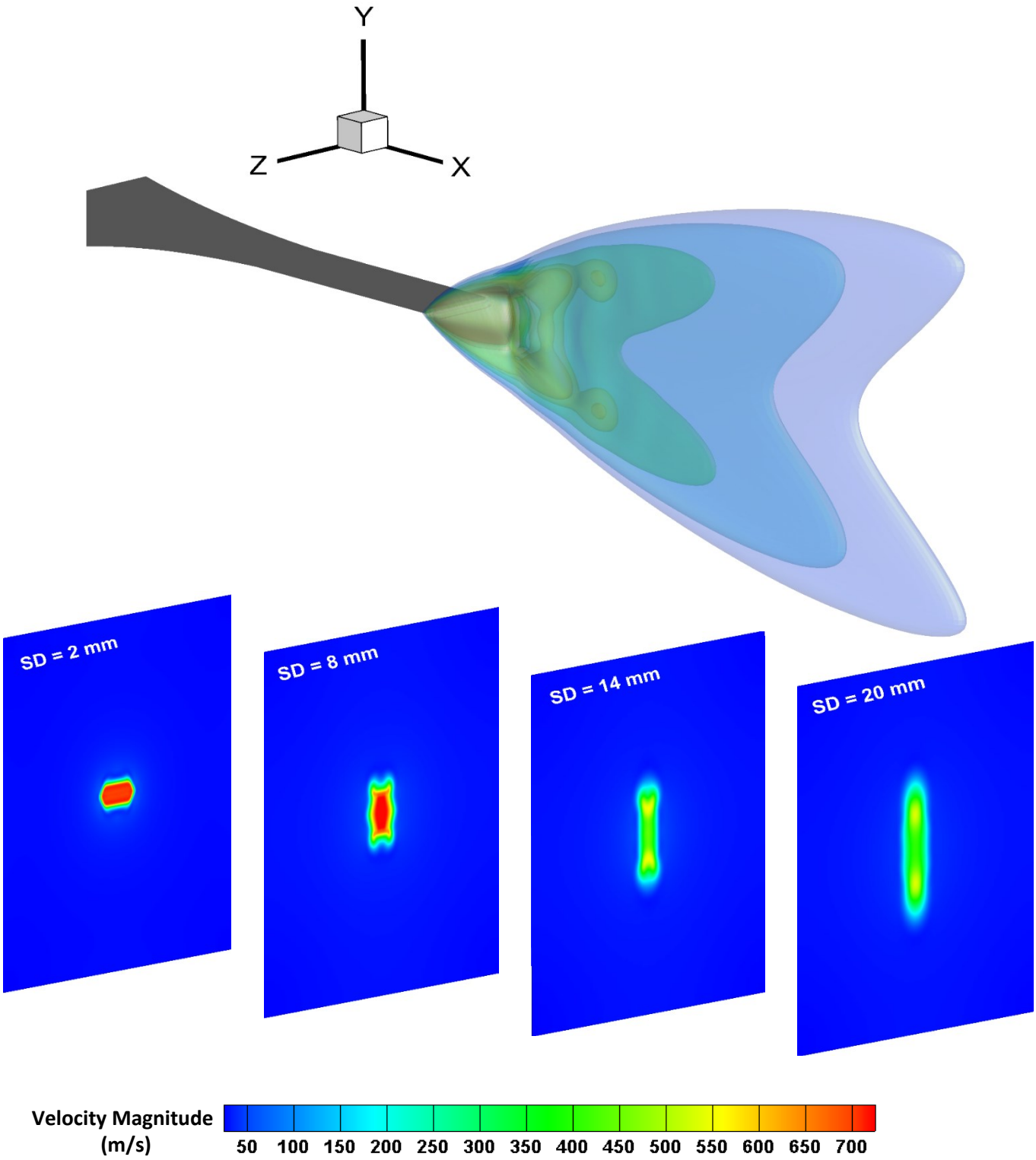

Figure 3.11 Velocity magnitude Iso-surface and slices at different distance from nozzle exit
SD: Standoff distance

These two phenomena are also studied by Grinstein [43] shown in Figure 3.12 for the study on vortex dynamics and entrainments in rectangular free jets [43].

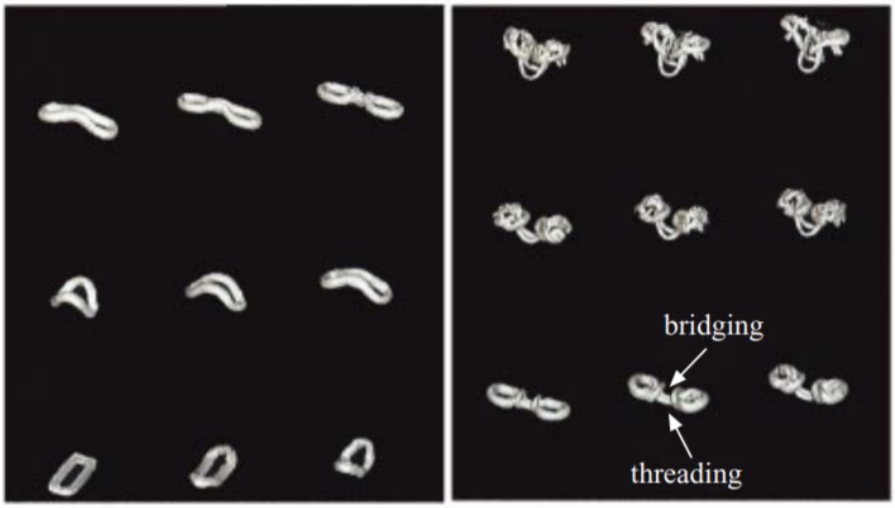

Figure 3.12 Axis-switching and bifurcation in rectangular free jets [43]

3.2.3. Effect of gas flow rate

The focus of this study is to investigate the effect of carrier gas flow rate on shock formation and velocity profile of the gas without presence of the substrate; therefore, the dependency of the flow characteristics including the velocity magnitude profile, Mach number and location of the shocks on carrier gas flow rate are presented in this section. To do so, the carrier gas flow rate is set to three different values of 2.5, 5 and 7.5 L/min. Where, the contours of velocity magnitude and Mach number for each of these flow rates are presented in Figures 3.13 (a)-(c) and 3.14 (a)-(c) as follows.

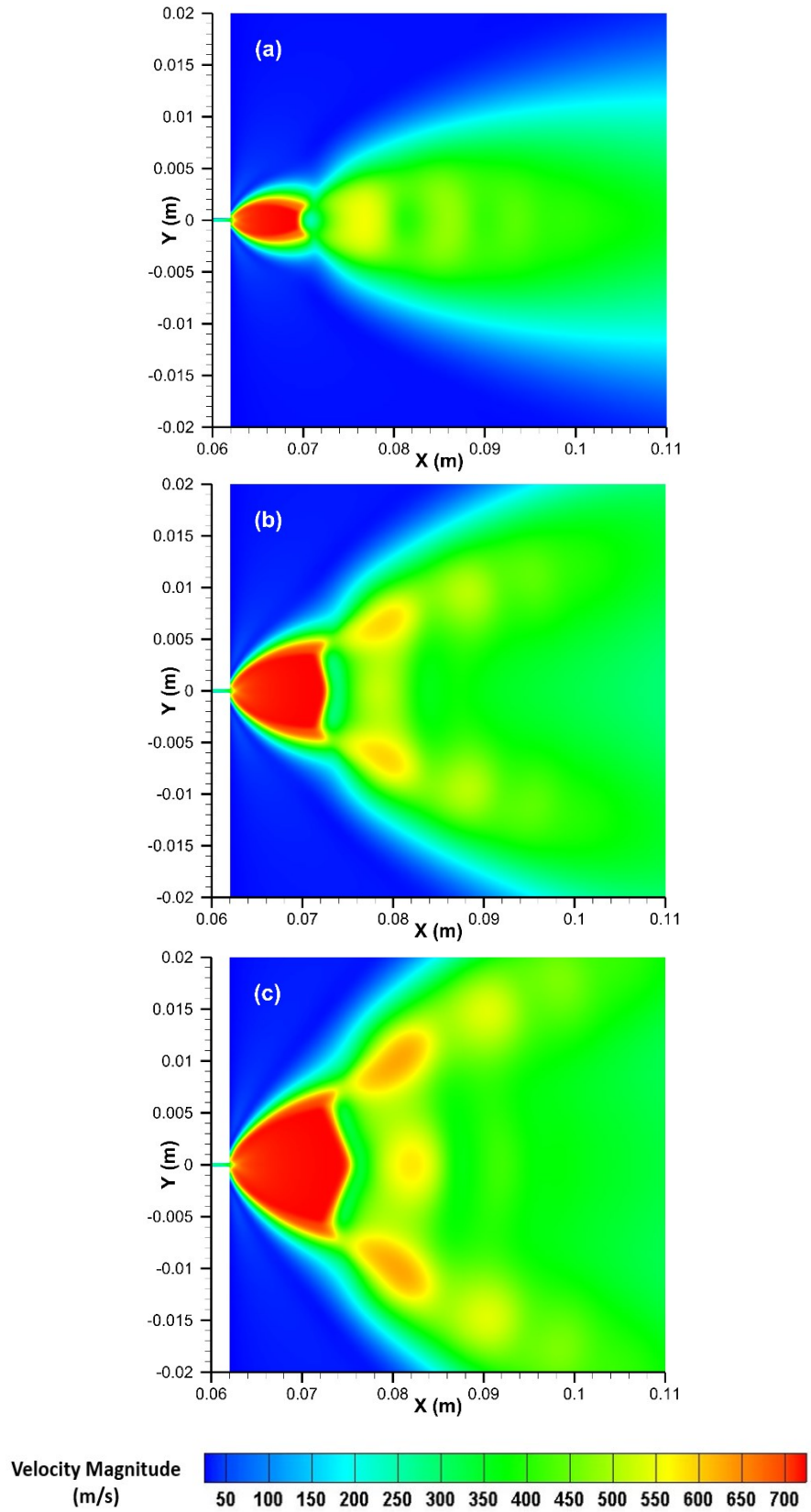

Figure 3.13 Contours of velocity magnitude for a) 2.5, b) 5 and c) 7.5 L/min flow rate

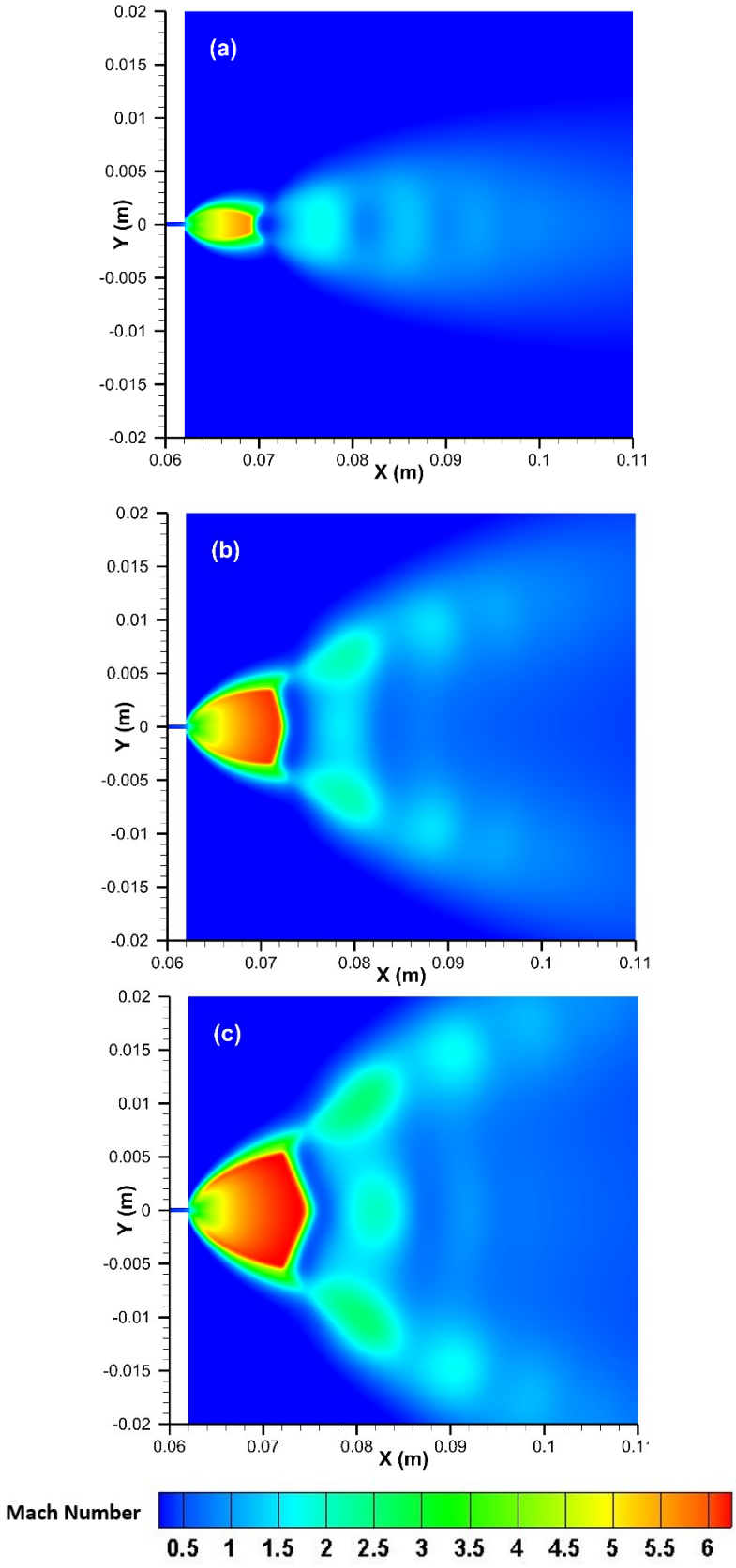

Figure 3.14 Contours of Mach number for a) 2.5, b) 5 and c) 7.5 L/min flow rate

It can be concluded that the velocity magnitude does not change significantly in the near field of the nozzle by changing the gas flow rate, where the maximum velocity of the gas is in the same range for these three flow rates. While the expansion ratio of the gas after the nozzle is a function of gas flow rate. On the other hand, the Mach number and shock locations change significantly with the gas flow rate. Therefore, the compressibility effect becomes dominant by increasing the gas flow rate. These facts have been discussed in validation section based on the experimental analysis presented for highly under-expanded jets by Crist et al. [24] for circular jets. Here it is shown that, for non-circular nozzles the Mach number and Mach disk distance is proportional to the gas flow rate like circular sonic nozzles

Since the aerosol moves along the centerline of the nozzle, most of the particles are in-flight around the area of centerline. Hence, the value of gas velocity and Mach number along the centerline is important to know. In order to show the relation between the gas velocity and Mach disk location at the centerline, both velocity and Mach number are plotted in Figure 3.15 (a)-(b). It can be inferred that, the behaviour of gas flow is independent of its flow rate before the Mach disk location associated with the minimum flow rate shown in blue. This means that, once the Mach disk happens, the flow characteristics are highly dependent on gas flow rate. It can be also seen that, the Mach disk location is shifted to longer distance from nozzle exit plane and become stronger due to more pressure gradient between inlet and outlet boundaries.

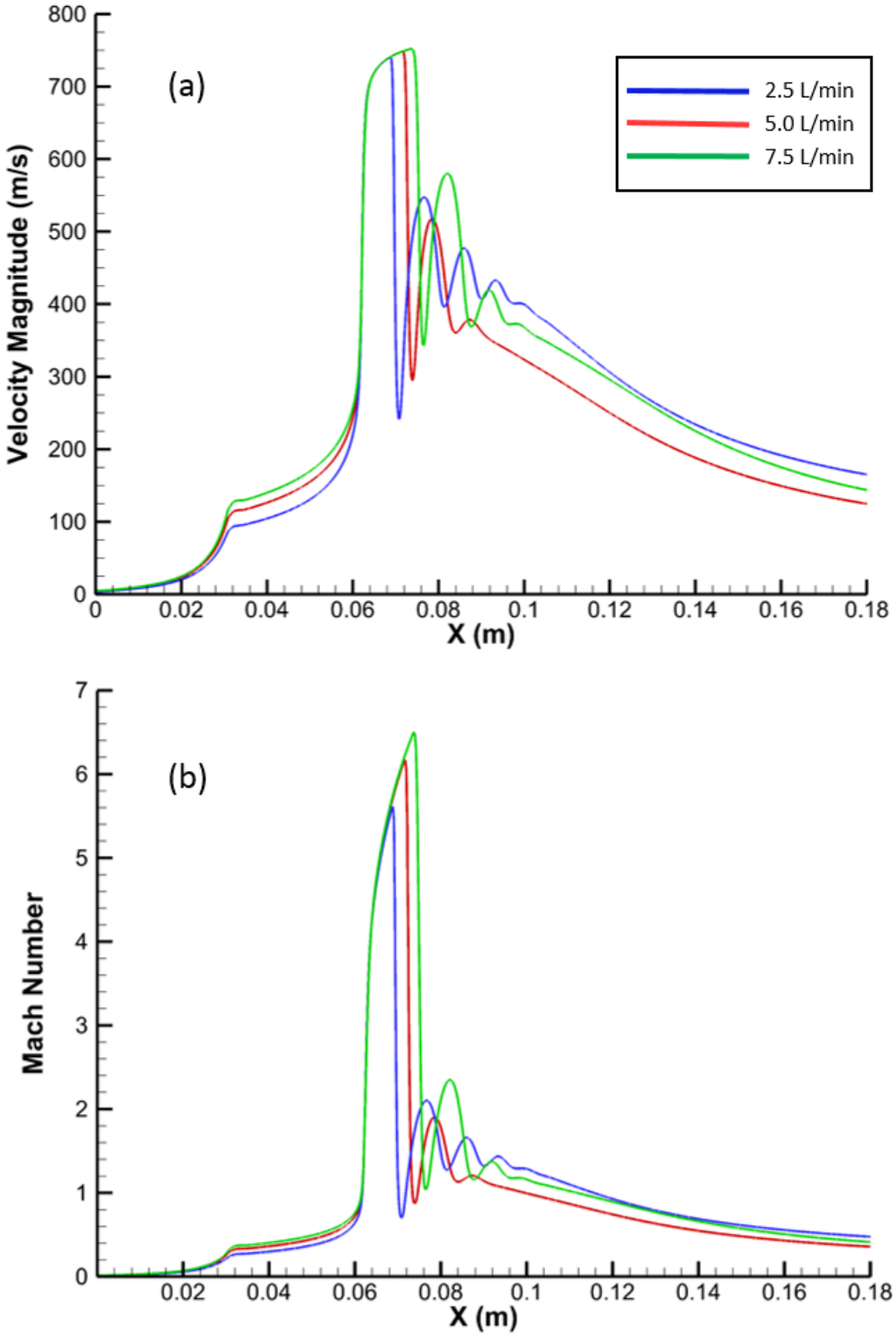

Figure 3.15 Effect of gas flow rate on velocity magnitude and Mach number in centerline

3.2.4. Effect of standoff distance

In this section, the effect of substrate distance from the nozzle known as standoff distance is studied for 4, 8 and 16 mm distances while, the Nitrogen gas consumption is 5 L/min and the pressure inside the deposition chamber is 150 Pa.

The 3D view of the gas profile for each case is presented in Figures 3.16.

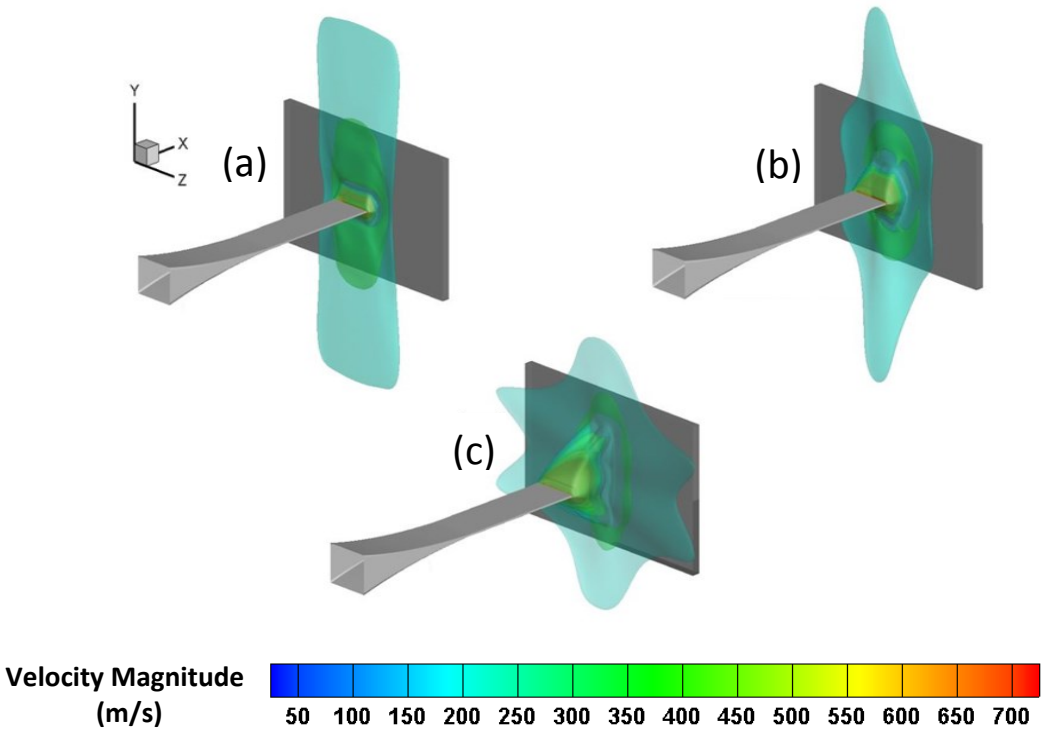

Figure 3.16 Iso-surface of impinging jet with different standoff distances a) 4, b) 8 and c) 16 mm

It can be concluded from Figure 3.16 that, the effect of axis-switching is more dominant for longer standoff distances. Longer distance allows the jet to expand across the minor axis of the nozzle; therefore, the profile of the gas is closer to the gas profile associated with the free jet case. Figures 3.17 and 3.18 are served to illustrate the velocity magnitude of the jet and also the Mach number associated with each case.

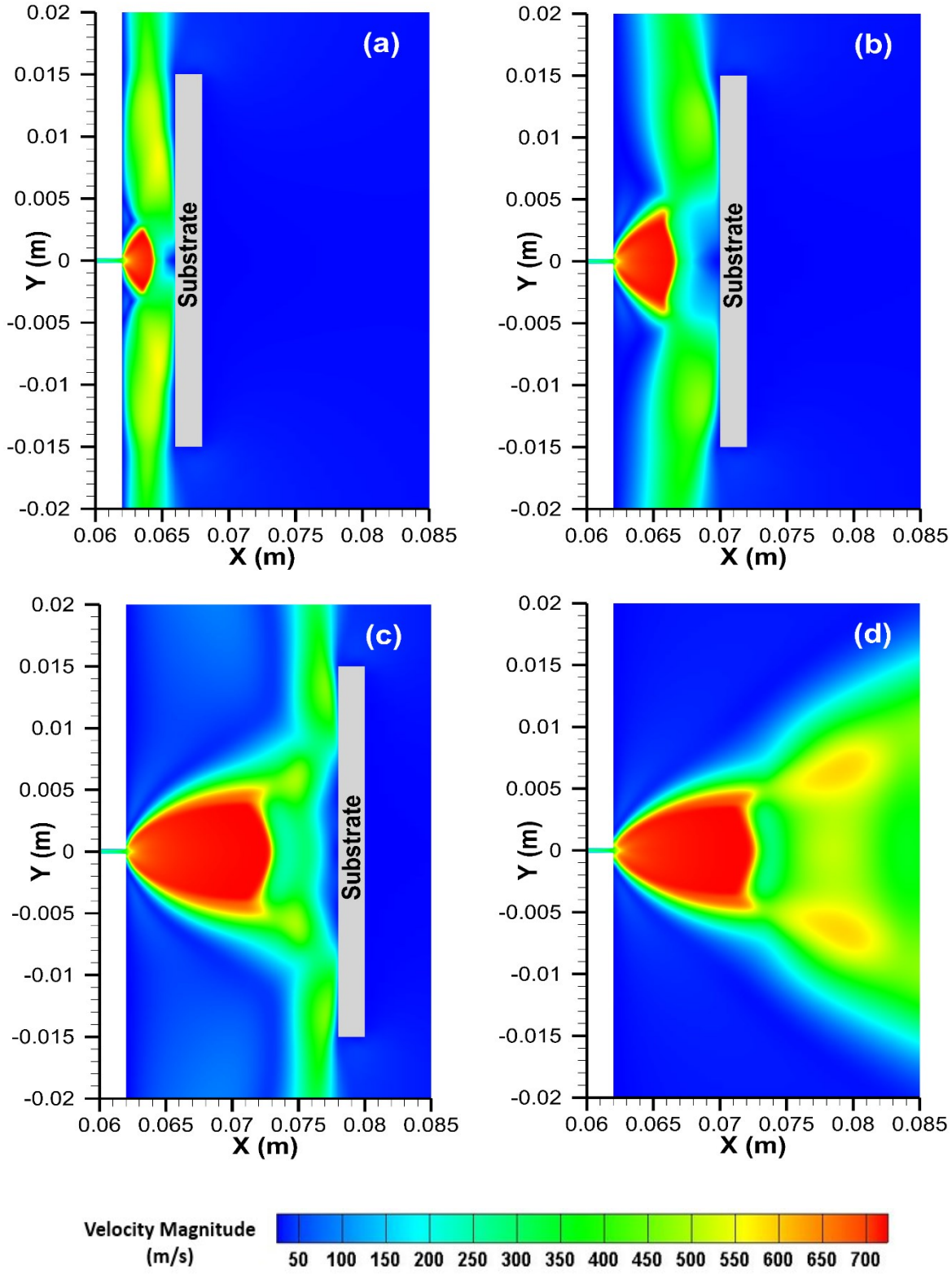

Figure 3.17 Contour of velocity magnitude for different standoff distances
a) 4, b) 8, c) 16mm and d) free jet

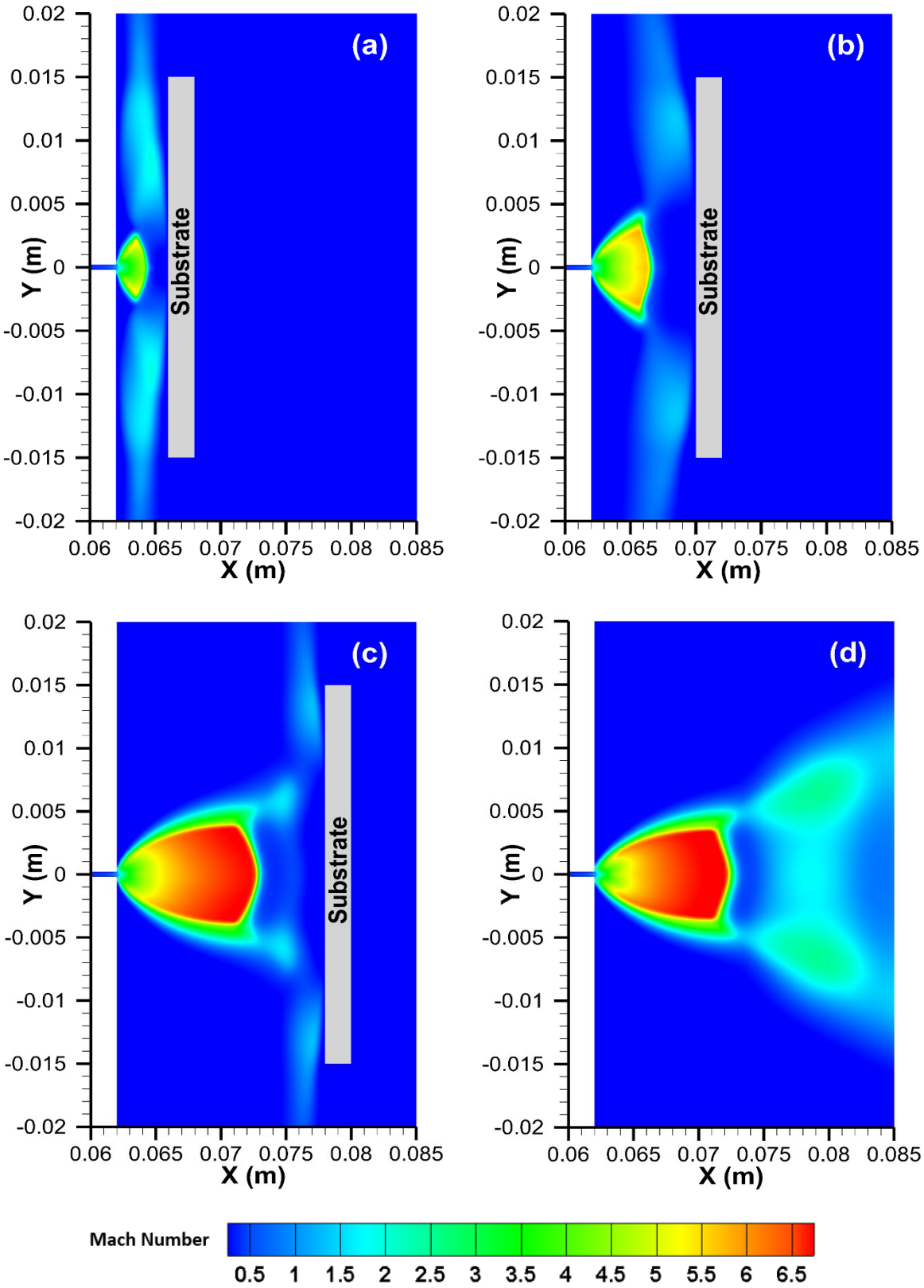

Figure 3.18 Contour of Mach number for different standoff distances
a) 4, b) 8, c) 16mm and d) free jet

According to the contours of velocity magnitude and Mach number, it can be inferred that the not only the jet profile but also the value of the velocity magnitude and Mach number is similar to the free jet case by increasing the standoff distance. In other word, the effect of substrate is negligible for long standoff distances.

The effect of substrate on particles trajectory is related to the effect of bow shock near the substrate; where the high pressure zone near the substrate apply a significant force to incoming particles. Hence, it is desire to evaluate the significance of this force by knowing the pressure gradient near the substrate.

The effect of bow shock at each three standoff distance are shown in Figures 3.19 (a)-(c) as follows. It can be concluded that, by increasing the standoff distance the effect of bow shock near the substrate becomes less and due to the axis-switching of the jet, the contour of pressure gradient near the substrate rotates 90 degree from figure 3.19 (a)-(c).

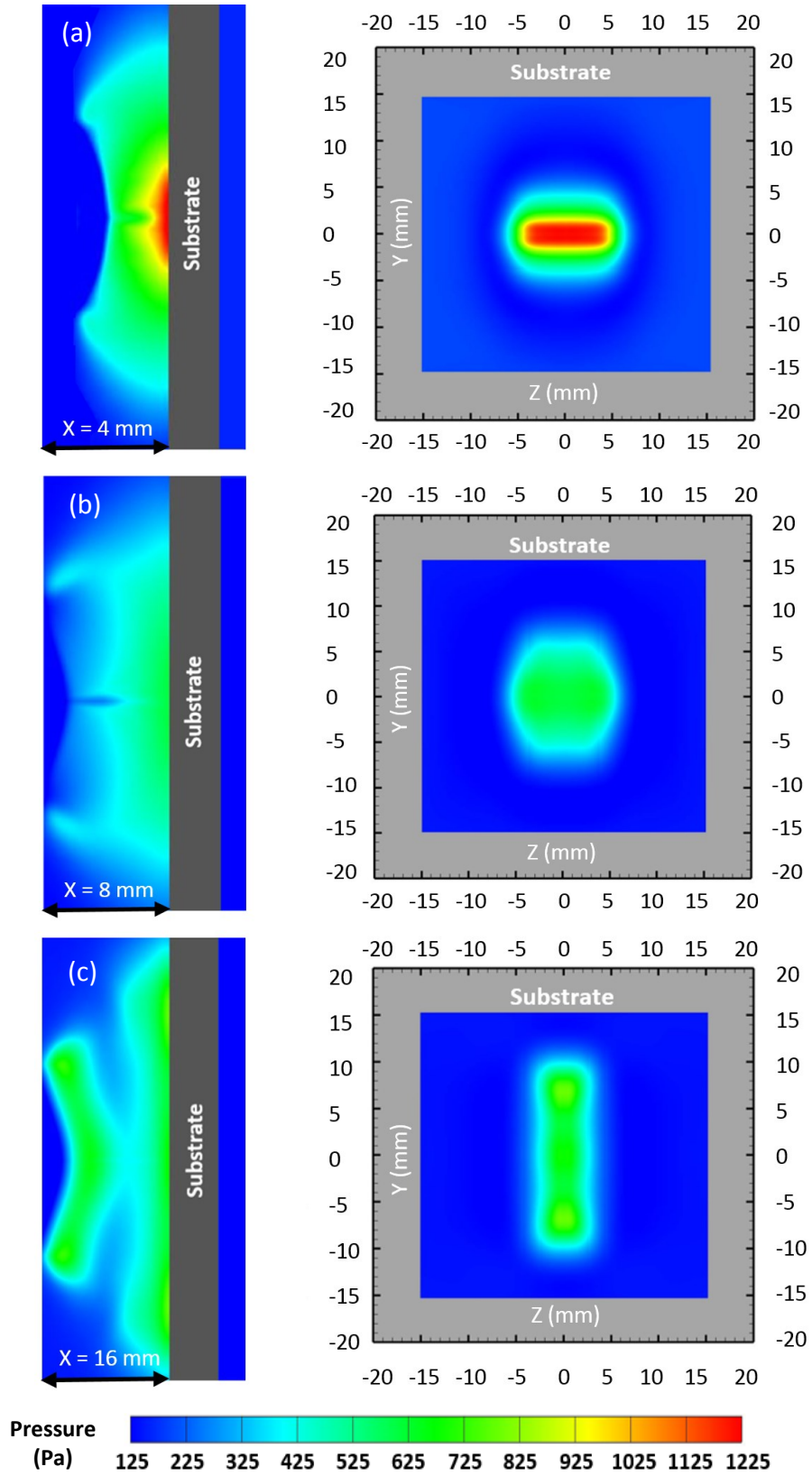

Figure 3.19 Contours of pressure on a flat substrate located at a) 4, b) 8, and c) 16 mm

The temperature gradient for each standoff distance is shown in figure 3.20 (a)-(c) as follows.

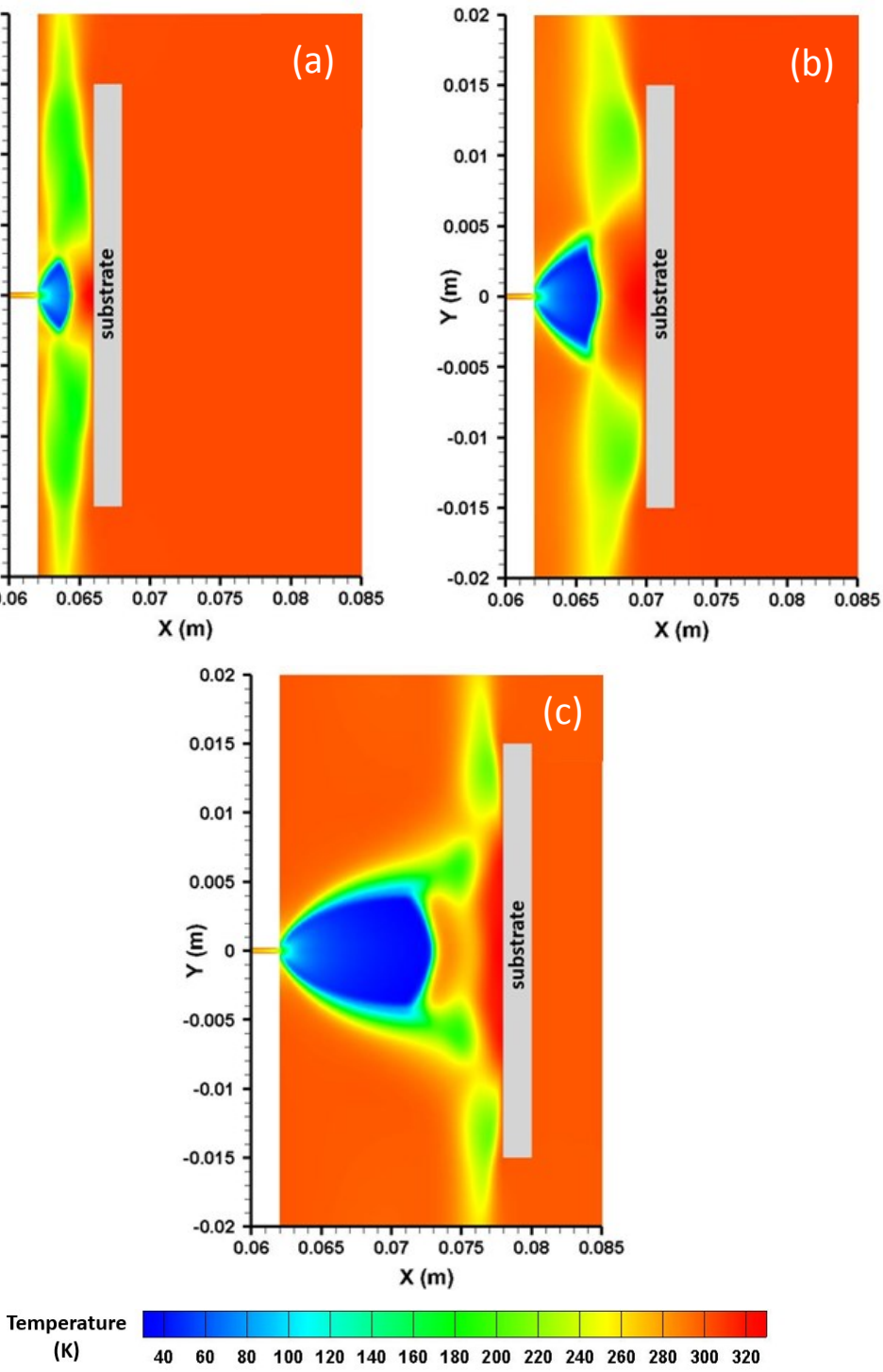

Figure 3.20 Contour of temperature for different standoff distances
a) 4, b) 8, and c) 16 mm

It can be concluded from figure 3.20 that, the spray process is associated with high temperature gradient in all three cases; therefore, the effect of Thermophoretic force is studied in the dispersed phase section.

3.3. Particle phase modeling

In this section, the effect of 3D analysis on in-flight particles velocity prediction is studied without presence of the substrate; then the effects of carrier gas flow rate, flat substrate and standoff distance on inflight particles behaviour are presented.

3.3.1. Comparison between 2D and 3D analysis

According to the gas flow modeling section, 3D analysis has significant influence on flow characteristic after the Mach disk; hence the in-flight particles velocity obtained from 3D model compare with the 2D model can be different depending on the standoff distance. In order to compare the results obtained from these two approaches, the average particles velocity for both cases are compared for two different standoff distances in Figures 3.21 (a – b) as follows.

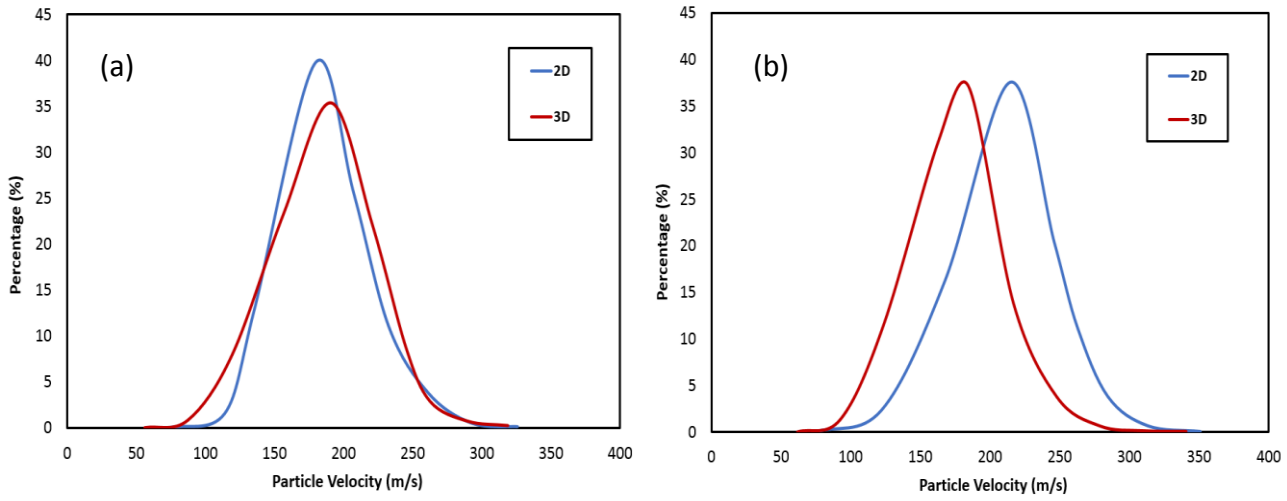

Figure 3.21 Particle velocity distribution at a) 8 mm and b) 16 mm from nozzle exit

It can be inferred from Figure 3.21 that, the difference between the results of 3D model become more by increasing the standoff distance. One can explain that, this difference is a consequence of different flow prediction after the Mach disk. According to the Experimental data for particles velocity from Naoe et al. [13], It can be seen that the predicted particles velocity from 3D model is closer to the measured velocity compare with the 2D planar model.

3.3.2. Effect of gas flow rate

According to gas flow modeling section, gas flow rate has significant influence on velocity profile and Mach number of the carrier gas; therefore, it can affect the in-flight particles during the spray process. Therefore, particles trajectory during the process are shown in figure 3.22, showing the effect of carrier gas flow rate on in-flight particles velocity.

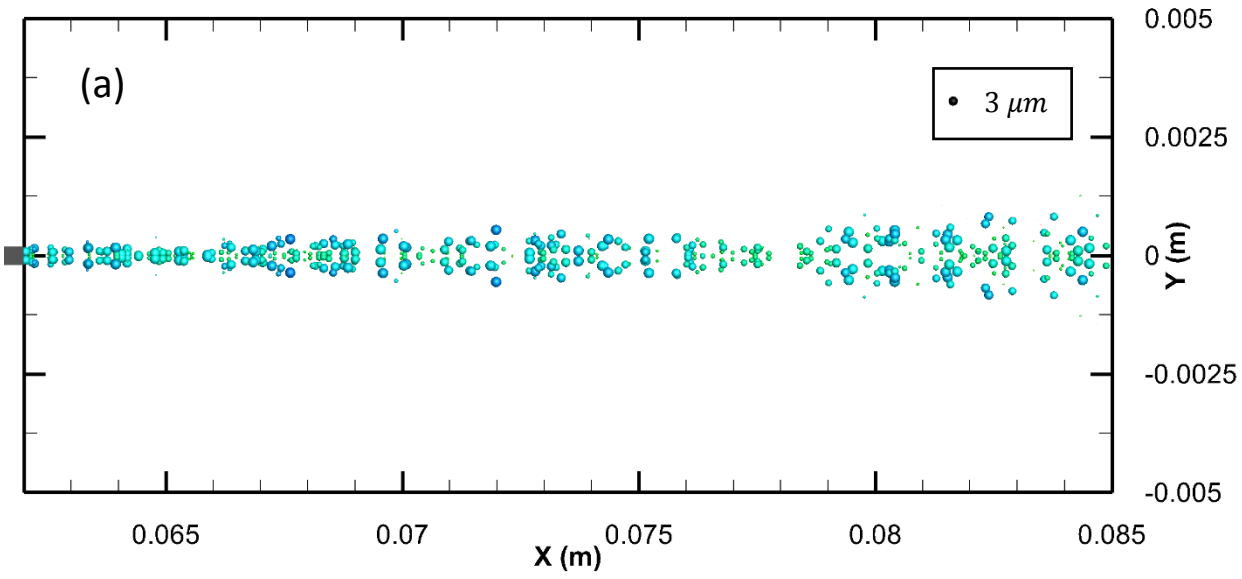

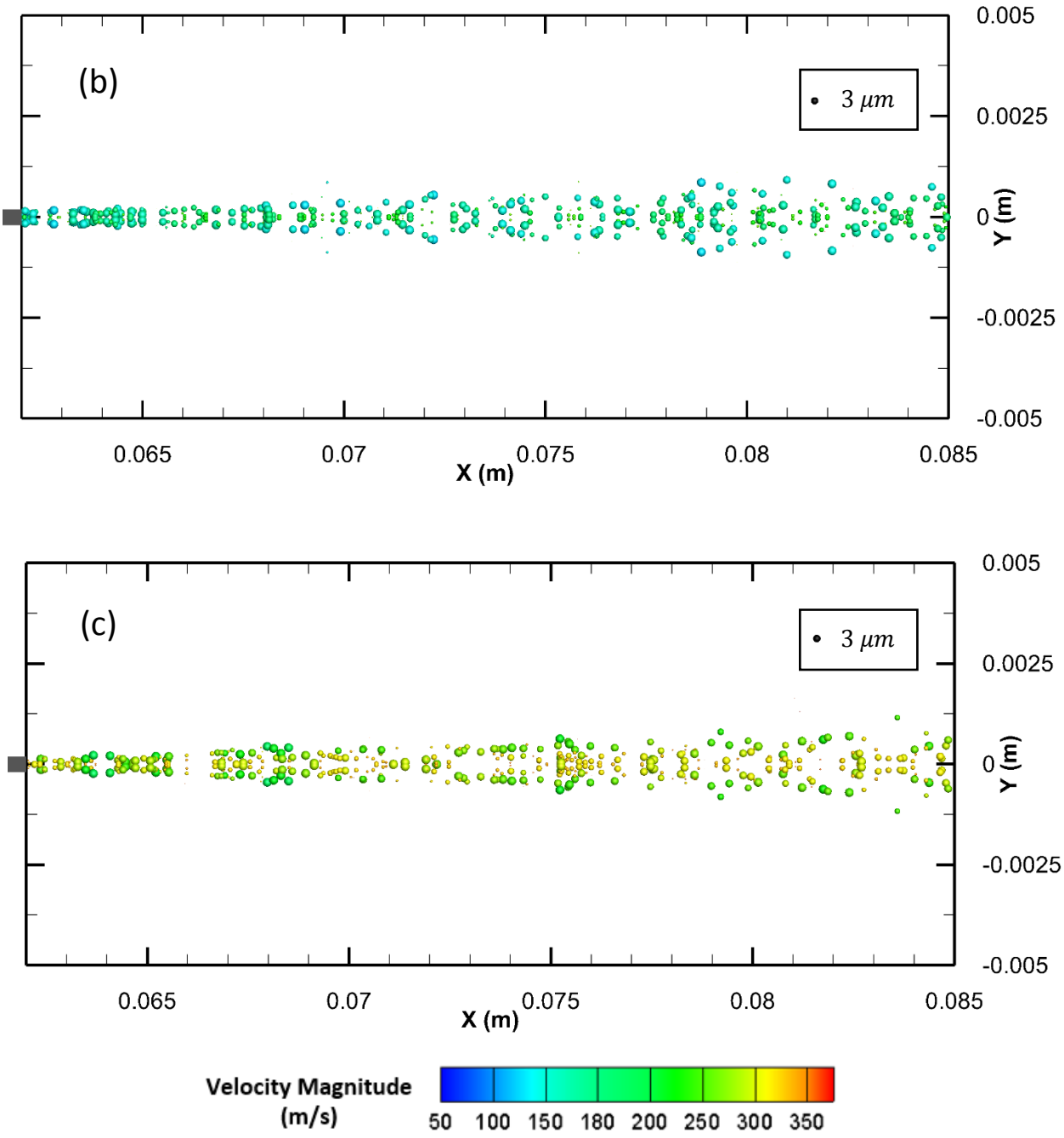

Figure 3.22 In-flight particles trajectory and velocity for different gas flow rates a) 2.5, b) 5 and c) 7.5 L/min

It can be inferred from the particles trajectory that, the velocity magnitude of the in-flight particles are proportional to their carrier gas flow rate. Moreover, the velocity of the smaller particles is always higher than large particles, since the applied force from the carrier gas to the

particles are identical and the effect of this force is adverse on small particles leading to more acceleration. In order to be more precise in terms of in-flight particles velocity, their distributions are plotted for different gas flow rates in Figure 3.23 and their velocity data including the maximum, mean and minimum velocity are reported in Table 3.3 as follow.

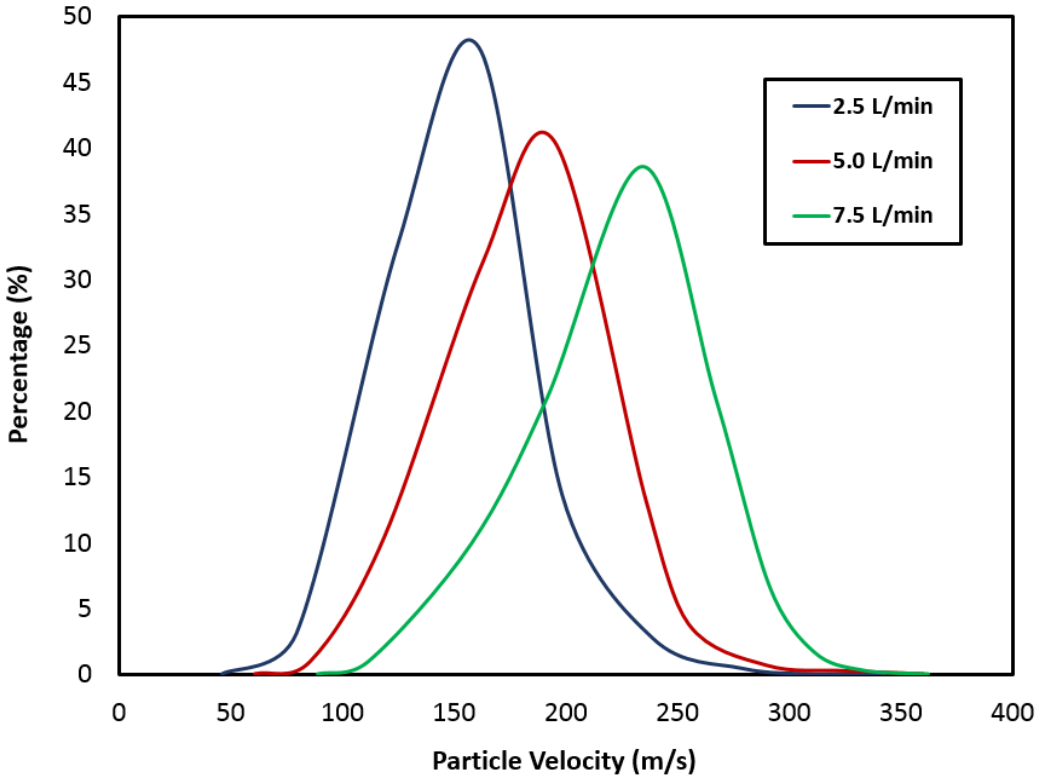

Figure 3.23 Particles velocity distribution for different gas flow rates

$\dot{V}_{gas}$ / $V_{particle}$	$2.5\ L/min$	$5\ L/min$	$7.5\ L/min$
Minimum	67 m/s	74 m/s	89 m/s
Mean	162.6 m/s	190 m/s	221 m/s
Maximum	340 m/s	360 m/s	362 m/s

Table 3.3 Particle velocity distribution based on gas flow rate

3.3.3. Effect of standoff distance

In aerosol deposition process, the most important parameter that can affect the deposition of ceramic particles is their kinetic energy upon impact which brings the attentions to the normal velocity impact of the particles. To see the effect of standoff distance on normal impact of the particles, a flat rectangular substrate as it mentioned in gas flow modeling section is located at 4 mm, 8mm and 16 mm far from the exit of the nozzle with a consistent gas flow rate of 5 L/min for each case. According to the gas flow modeling, the bow shock near the substrate can decelerate the particles impact velocity which can be seen in Figures 3.24 showing the in-flight particles velocity from the nozzle exit to the substrate. It can be inferred from Figures 3.24 that, the average in-flight particles velocity for all cases are in the same range and there is no significant change happens for the kinetic energy of the particles. This fact can be explained based on the low pressure gradient that is associated with this coating process, where the pressure difference from the expansion region and bow shock region near the substrate is quite the same and small for different cases. This figure verifies that the particle normal velocity is independent of substrate location and standoff distance, since the particles' Stokes number are on the order of magnitude of 1000. According to other papers [44]–[46], the Stokes number is defined as $St = 4m_p u_p / 6\pi\mu_g {d_p}^2 = \rho_p d_p u_p / 9\mu_g$ (where ρ_p is the particle density) which is the ratio of the particle's inertia and the drag force. Therefore, a particle with lower Stokes number follows the gas streamlines while, a particle with higher Stokes number is not affected significantly by the gas flow and tracks its own trajectory. In this figure, the particle velocity profile for a free jet (without substrate) at 8 mm from the nozzle exit is also illustrated. It clarifies that the substrate presence causes the particle velocity to reduce slightly, owing to occurrence of the bow shock and the stagnation region.

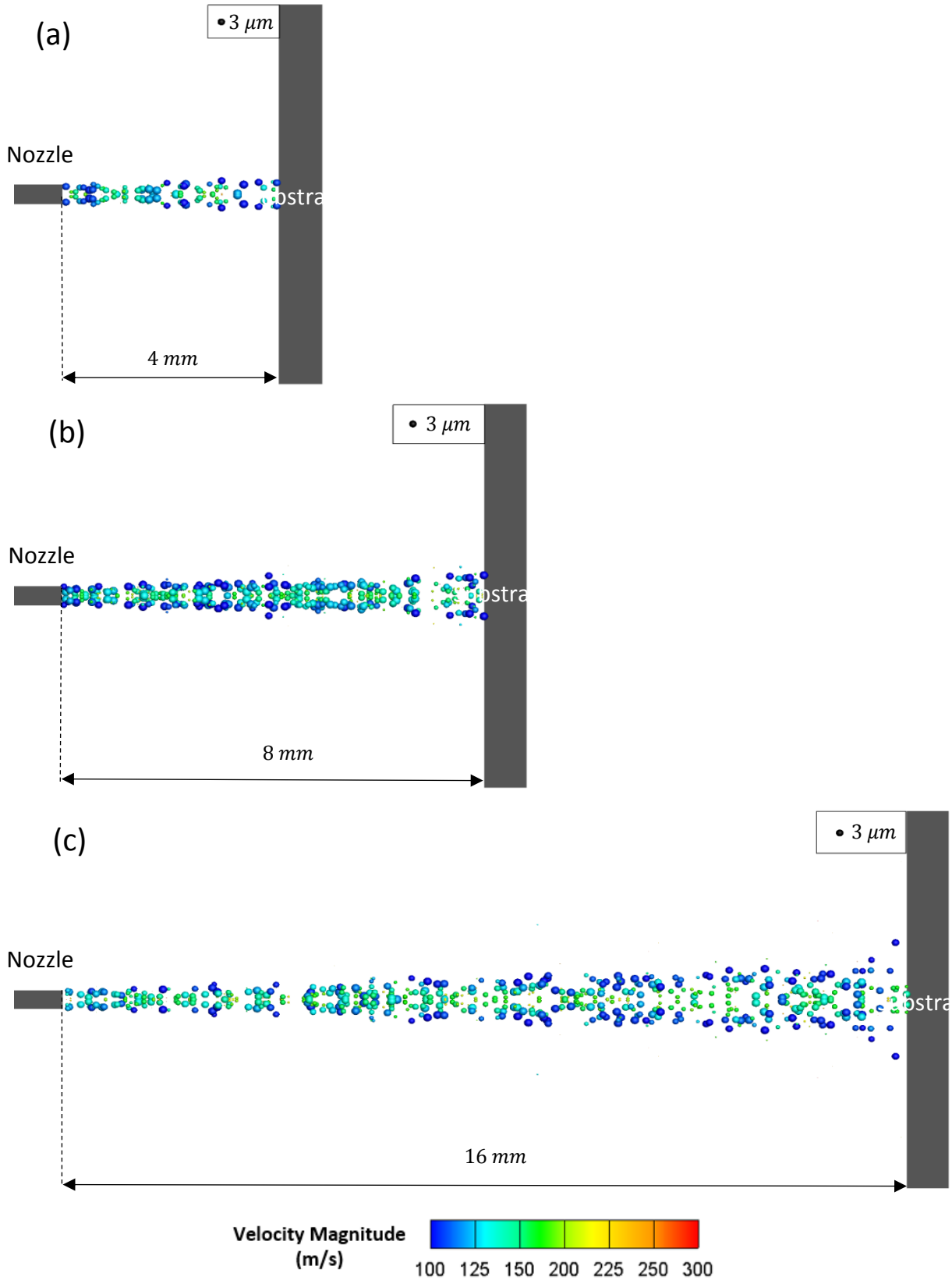

Figure 3.24 Particles trajectory at XY plane for different standoff distance
a) 4, b) 8 and c) 16 mm

Since the normal velocity upon impact is an important data, the distribution of normal velocity upon impact for different standoff distances are plotted as well as the normal impact velocity at 8mm from the nozzle exit without the presence of the substrate.

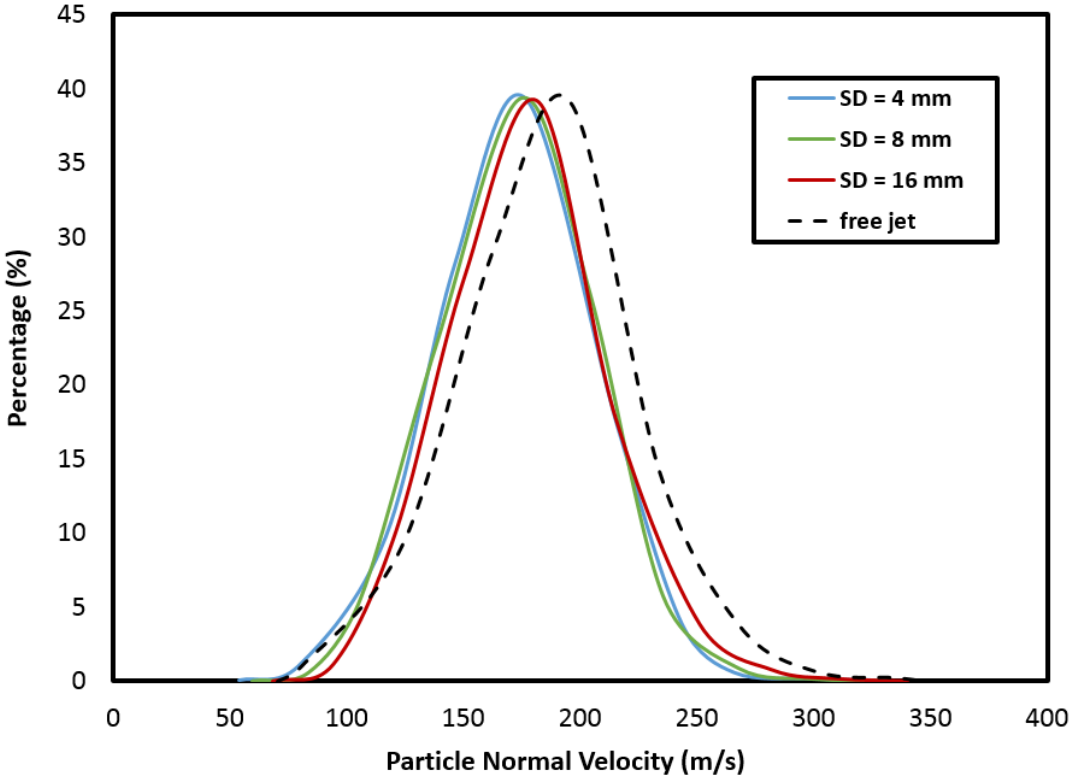

Figure 3.25 Normal velocity distribution for different standoff distances and Free-jet at 8 mm from the nozzle exit

It can be concluded from this graph that, although the bow shock near the substrate reduces the particles normal velocity upon impact by less than 10 % compare to the free-jet spray condition; the effect of standoff distance on normal velocity of the particles are negligible due to the negligible effect of the bow shock in aerosol deposition process. In order to show the particles distribution at the substrate for different standoff distances, their distributions are displayed in Figure 3.26, where the gas flow rate are equal to 5 L/min and consistent for all three cases.

Particles' landing locations are presented in Figure 3.26 for different standoff distances. To study the effect of bow shock on particles trajectory and impact velocity. For this section, only particles smaller than 4 μm are presented due to the negligible percentage of larger particles and the fact that larger particles cannot be deposited.

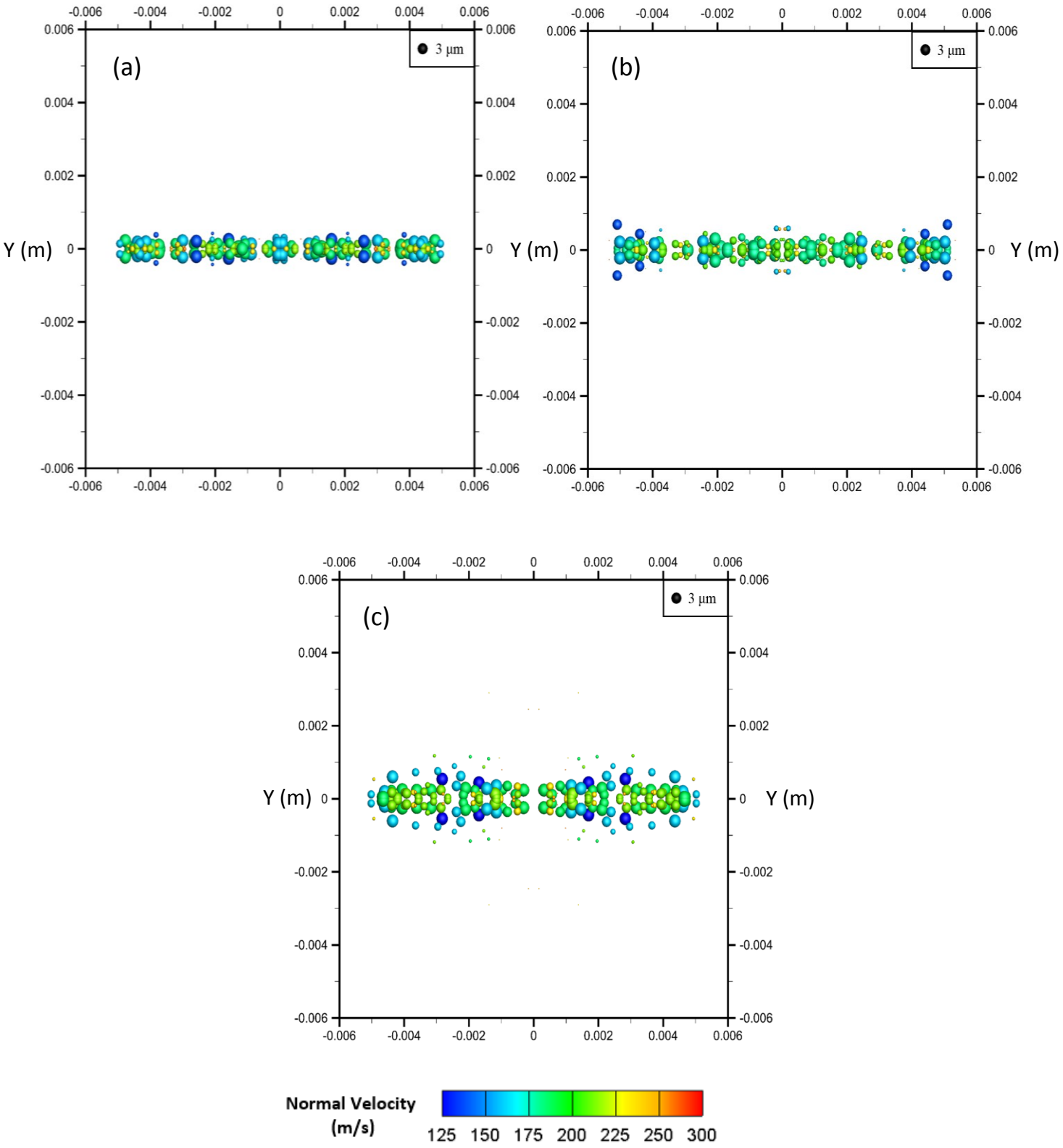

Figure 3.26 Particles distribution at the substrate for a) 4 b) 8 and c) 16 mm standoff distances

According to Figure 3.26 (a), particles landing locations are located along the major axis of the slit nozzle. Since the axis-switching happens in far distance from the exit of the nozzle, most of the particles are locating near to the major axis. Therefore; at 4 mm from the nozzle's exit, all particles are landed near the major axis of the nozzle. Moreover, small particles are distracted from the center of the jet due to the bow shock near the substrate. It can be inferred from Figure 3.26 (b) that, particles landing locations are closer to the minor axis of the nozzle because, the carrier gas has more distance for the axis-switching but, according to Figure 3.19 (b), the axis-switching phenomena is not completed when the substrate is located at 8 mm and the bow shock pattern is quite uniform in both directions. Therefore, particles are less distracted from the center of the substrate. Moreover, deceleration of the particles near the substrate are less due to the reduction of bow shock strength. Finally at 16 mm from the nozzle's exit, the axis-switching is completed and more particles are distracted from the center of the substrate although, the significance of the bow shock is less compare with the previous standoff distances. In other word, the axis-switching of the jet is affected the particles trajectory and deviated them from the center of the jet toward the minor axis direction.

To conclude, only particles with enough kinetic energy can remain around the centerline and the rest are distracted due to the shocks mainly near the substrate. Therefore, particles size distribution is important parameter because having large particles results in lower velocity and small kinetic energy; on the other hand, small particles also have low kinetic energy due to their low mass and can be easily distracted although their velocities are high. This phenomena is explained based on the definition of Stokes number in previous section as well. The best size distribution range for the particles according to Figure 3.26, approximately starts from minimum 1 μm to 4 μm in maximum case.

3.3.4. Effect of Thermophoretic force

According to the significant temperature gradient due to the impingement of the jet with the substrate, the effect of thermophoretic force is shown in Figure 3.27 as follow only for 8 mm different standoff distance.

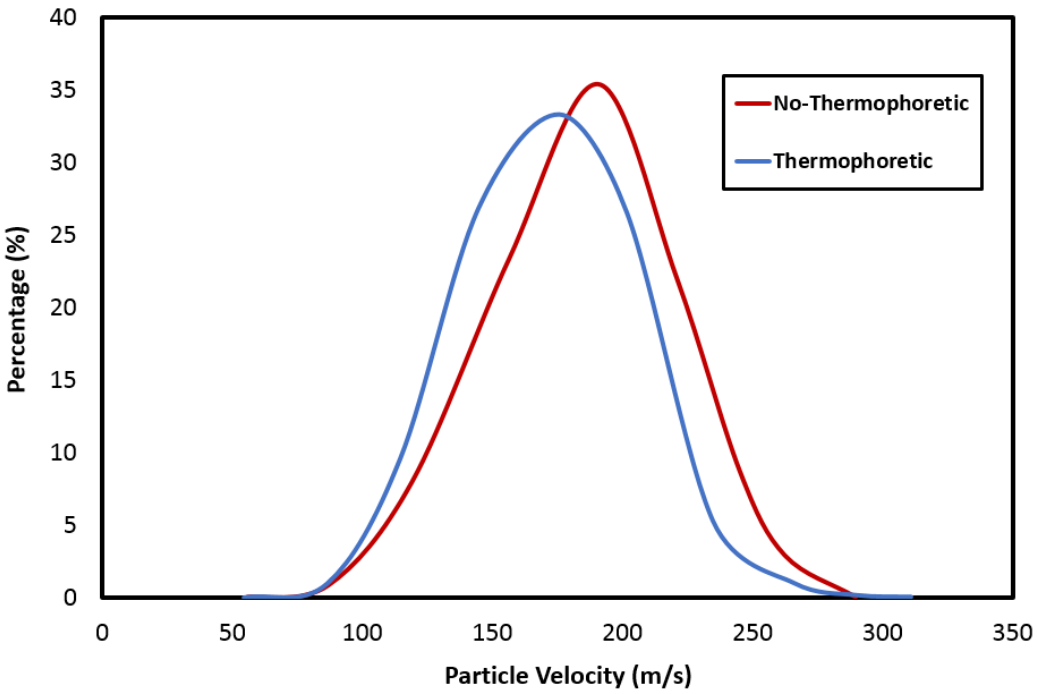

Figure 3.27 Distribution of particles normal velocity upon impact with and without considering the effect of thermophoretic force

It can be inferred from the graph that due to the temperature gradient at the substrate location, there is a slight deceleration on particles normal velocity upon impact approximately for particles with 125 - 225 m/s particles velocity. According to the Talbot [37] correlation, the key parameters for thermophoretic force are particles mass, temperature gradient and thermophoretic coefficient, which itself is a function of particles size. By incorporating the thermophoretic force effect in the model, it is concluded from Figure 3.26 that large particles with 5 μm diameter and above have lower velocity(i.e. approximately below 150 m/s), while

small particles below 1 μm have higher normal velocity approximately over 225 m/s. This means that in figure 3.27, the effect of thermophoretic force is rather small for the large particles in lower range of velocity and also negligible for the higher range of velocities because, particles existing in this range have small diameter which decrease the value of thermophoretic coefficient.

4. Conclusion and Future work

Overview

In this chapter, the conclusion of this study is presented and future work for numerical study in aerosol deposition technology are proposed.

In this numerical study, the effect of compressibility and rarefaction of the carrier gas (Nitrogen) on solid particles (e.g. Al_2O_3) velocity and trajectory are studied by implementing Schiller-Naumann [38] and Loth [39] drag expressions in a 2D planar geometry. The numerical results show that the expression presented by Loth is the more accurate one due to the inclusion of particle Knudsen, Mach and Reynolds numbers resulted in a very good agreement with the experimental results in the literature. Consequently, the 3D geometry is proposed instead of 2D planar model to capture the complex 3D fluid flow features outside the nozzle and near the substrate. It is observed that, the result of 2D is close to the 3D one before the Mach disk but, afterward there exists a significant difference between the 3D and 2D results. Moreover, the 3D analysis shows the axis-switching and Mach disk location which is not possible to capture in 2D planar model.

Special attention was paid in this study to investigate the effect of carrier gas flow rate on the in-flight particles velocity. It is concluded that by increasing the gas flow rate from 2.5 to 7.5 L/min, particles velocity increase by about 100 m/s.

The effect of substrate and standoff distance on normal velocity of the particles upon impact are also studied in this work by locating the substrate at 4, 8 and 16 mm from the exit of the nozzle with 5 L/min constant gas flow rate. The normal velocity of the particles with the substrate compare with the normal velocity of the particles at the same distance in free-jet show that the bow shock near the substrate reduces the particles normal velocity by 10 %, while changing the substrate location does not make significant change on particles normal velocity. It is explained that the vacuum condition and low pressure gradient inside the deposition chamber causes this situation and minimized the effect of bow shock and deceleration of the particles.

Finally, the effect of thermophoretic force on particles normal velocity upon impact is also discussed in this work based on the high temperature gradient associated to aerosol deposition coating process. It is concluded that, this effect is only sensible for particles in a certain range of velocity based on their mass and diameter which means that for large particles and also for ultra-fine particles with small diameter, this phenomenon does not have a significant impact.

The complexity level of aerosol deposition process including the pressure inside the deposition chamber, particles shape and numerical approach for this physical process, have made it difficult to come up with a unique method of simulation. However, there are some future steps to improve the existing model and also other phenomena that play roles during the process. Some of these steps are summarized as follows.

- In this study, it is assumed that the pressure inside the deposition chamber is high enough that the flow can be considered in continuum region and Navier-Stokes equations are valid for the numerical modeling. However, by operating system in low pressures below 0.1 torr the flow in some areas may act as free-molecular regime which means that Boltzmann equations should be used for the gas flow modelling.
- In terms of turbulence study, different turbulence models can be compared with each other for both free-jet and impinging jet modeling.
- For the solid particles phase, the existing model assumed all particles to be perfectly spherical; therefore, future step could be done for the study of particles shape on their in-flight and normal impact velocity.
- The effect of nozzle geometry mainly for the shape of their cross section on particles velocity and distribution can be considered as a potential future study.

References

[1] P. L. Fauchais, J. V. R. Heberlein, and M. I. Boulos, Thermal Spray Fundamentals. 2014.

[2] Schematic of Cold Spray System. (2018, 10 August) Retrieved from https://www.mtec.or.th/en/cold-spray2-2/

[3] E. Irissou, J.-G. Legoux, A. N. Ryabinin, B. Jodoin, and C. Moreau, "Review on Cold Spray Process and Technology: Part I—Intellectual Property," J. Therm. Spray Technol., vol. 17, no. 4, pp. 495–516, 2008.

[4] T. Schmidt et al., "From particle acceleration to impact and bonding in cold spraying," J. Therm. Spray Technol., vol. 18, no. 5–6, pp. 794–808, 2009.

[5] D. Hanft, J. Exner, M. Schubert, T. Stocker, P. Fuierer, and R. Moos, "An Overview of the Aerosol Deposition Method: Process Fundamentals and New Trends in Materials Applications," J. Ceram. Sci. Technol., vol. 6, no. 3, pp. 147–181, 2015.

[6] J. Akedo, "Room temperature impact consolidation (RTIC) of fine ceramic powder by aerosol deposition method and applications to microdevices," J. Therm. Spray Technol., vol. 17, no. 2, pp. 181–198, 2008.

[7] J. Akedo, "Aerosol deposition of ceramic thick films at room temperature: Densification mechanism of ceramic layers," in Journal of the American Ceramic Society, 2006, vol. 89, no. 6, pp. 1834–1839.

[8] J. Akedo, "Aerosol Deposition Method for Room-Temperature Ceramic Coating and Its Applications," in Handbook of Advanced Ceramics: Materials, Applications, Processing, and Properties: Second Edition, 2013, pp. 847–860.

[9] M. Furt, “Capstone (final report),” no. 25977002, 2016.

[10] S. Kong, F. Application, and P. Data, “(12) United States Patent,” vol. 2, no. 12, pp. 12–15, 2011.

[11] M. W. Lee et al., “Optimization of supersonic nozzle flow for titanium dioxide thin-film coating by aerosol deposition,” J. Aerosol Sci., vol. 42, no. 11, pp. 771–780, 2011.

[12] Y. Park et al., “Effect of gas flow rates and nozzle throat width on deposition of α-alumina films of granule spray in vacuum,” J. Eur. Ceram. Soc., vol. 37, no. 7, pp. 2667–2672, 2017.

[13] K. Naoe, M. Nishiki, and A. Yumoto, “Relationship between impact velocity of Al2O3 particles and deposition efficiency in aerosol deposition method,” in Journal of Thermal Spray Technology, 2013, vol. 22, no. 8, pp. 1267–1274.

[14] K. Naoe, K. Sato, and M. Nishiki, “Effect of process for producing Al 2 O 3 particles on deposition ef fi ciency in aerosol deposition method,” 2014.

[15] J. J. Park et al., “Supersonic nozzle flow simulations for particle coating applications: Effects of shockwaves, nozzle geometry, ambient pressure, and substrate location upon flow characteristics,” J. Therm. Spray Technol., vol. 20, no. 3, pp. 514–522, 2011.

[16] S. D. Johnson, D. Schwer, D. S. Park, Y. S. Park, and E. P. Gorzkowski, “Deposition efficiency of barium hexaferrite by aerosol deposition,” Surf. Coatings Technol., vol. 332, pp. 542–549, 2017.

[17] H. Katanoda and K. Matsuo, “Gasdynamic Simulation of Aerosol Deposition Method,” Mater. Trans., vol. 47, no. 7, pp. 1620–1625, 2006.

[18] J. F. O'Hanlon, A User's Guide to Vacuum Technology. 2003.

[19] J. H. Moore, C. C. Davis, M. A. Coplan, and S. C. Greer, Building scientific apparatus: Fourth edition, vol. 9780521878. 2009.

[20] Y. A. Çengel and J. M. Cimbala, "Fluid mechanics: fundamentals and applications," Fluid Mech. With Probl. Solut. an Aerodyn. Lab., p. 956, 2006.

[21] K. Y. R. Dabir S. Viswanath, Tushar K. Ghosh, Dasika. H. L. Prasad, Nidamarty V.K. Dutt, Viscosity of liquids. 2007.

[22] P. D. Neufeld, A. R. Janzen, and R. A. Aziz, "Empirical Equations to Calculate 16 of the Transport Collision Integrals Ω(l, s) for the Lennard-Jones Potential," J. Chem. Phys., vol. 57, no. 3, p. 1100, 1972.

[23] Inc. ANSYS, ANSYS FLUENT Theory Guide, vol. 15.0, no. November. 2012.

[24] S. CRIST, D. R. GLASS, and P. M. SHERMAN, "Study of the highly underexpanded sonic jet.," AIAA J., vol. 4, no. 1, pp. 68–71, 1966.

[25] J. Akedo and M. Lebedev, "Influence of Carrier Gas Conditions on Electrical and Optical Properties of Pb(Zr,Ti)O3 Thin Films Prepared by Aerosol Deposition Method," Jpn. J. Appl. Phys., vol. 40, no. Part 1, No. 9B, pp. 5528–5532, 2001.

[26] M. Lebedev, J. Akedo, K. Mori, and T. Eiju, "Simple self-selective method of velocity measurement for particles in impact-based deposition," J. Vac. Sci. Technol. A Vacuum, Surfaces, Film., vol. 18, no. 2, pp. 563–566, 2000.

[27] H. Katanoda, M. Fukuhara, and N. Iino, "Numerical simulation on impact velocity of ceramic particles propelled by supersonic nitrogen gas flow in vacuum chamber," Mater.

Trans., vol. 48, no. 6, pp. 1463–1468, 2007.

[28] J. Kwon, H. Park, I. Lee, and C. Lee, “Effect of gas flow rate on deposition behavior of Fe-based amorphous alloys in vacuum kinetic spray process,” Surf. Coatings Technol., vol. 259, no. PC, pp. 585–593, 2014.

[29] H. Park, H. Kwon, and C. Lee, “Inflight Particle Behavior in the Vacuum Kinetic Spray Process,” J. Therm. Spray Technol., vol. 26, no. 7, pp. 1616–1631, 2017.

[30] H. Park, J. Kim, S. B. Lee, and C. Lee, “Correlation of Fracture Mode Transition of Ceramic Particle with Critical Velocity for Successful Deposition in Vacuum Kinetic Spraying Process,” J. Therm. Spray Technol., vol. 26, no. 3, pp. 327–339, 2017.

[31] L. S. Wang et al., “Effect of the powder particle structure and substrate hardness during vacuum cold spraying of Al2O3,” Ceram. Int., vol. 43, no. 5, pp. 4390–4398, 2017.

[32] “An introduction to fluid dynamics. G. K. Batchelor, F.R.S., London (Cambridge University Press), 1967. Pp. xvii, 615; Plates 24; Numerous Figures. 75s. in U.K., $13.50 in U.S.A,” Quarterly Journal of the Royal Meteorological Society, vol. 94, no. 401. pp. 435–435, 1968.

[33] F. White, “Fluid Mechanics,” McGraw-Hill,New York, p. 862, 2010.

[34] V. J, R. M, and H. C, “On the use of wall functions as boundary conditions for two-dimensional separated compressible flows,” 23rd Aerosp. Sci. Meet., 1985.

[35] C. T. Crowe, J. D. Schwarzkopf, M. Sommerfeld, and Y. Tsuji, “Multiphase Flow with Droplets and Particles,” CRC Press Taylor Fr. Gr., p. 209, 2011.

[36] X. Chen, “Thermophoretic force acting on a small particle suspended in the near-wall

region of a low-pressure plasma processor," J. Phys. D. Appl. Phys., vol. 32, no. 16, pp. 2075–2082, 1999.

[37] L. Talbot, R. K. Cheng, R. W. Schefer, and D. R. Willis, "Thermophoresis of particles in a heated boundary layer," J. Fluid Mech., vol. 101, no. 4, pp. 737–758, 1980.

[38] L. Schiller and Z. Naumann, "A drag coefficient correlation," Z.Ver.Deutsch.Ing, vol. 77, no. 13–14, pp. 318–320, 1933.

[39] E. Loth, "Compressibility and Rarefaction Effects on Drag of a Spherical Particle," AIAA J., vol. 46, no. 9, pp. 2219–2228, 2008.

[40] S. Sivier, E. Loth, J. Baum, and R. Löhner, "Unstructured adaptive remeshing finite element method for dusty shock flow," Shock Waves, vol. 4, no. 1, pp. 15–23, 1994.

[41] A. Acrivos, "Bubbles, Drops and Particles. By R. C LIFT , J. R. G RACE and M. E. W EBER . Academic Press, 1978. 380 pp. £20.80 or $32.00.," J. Fluid Mech., vol. 94, no. 04, p. 795, 1979.

[42] P. S. Epstein, "Zur Theorie des Radiometers," Zeitschrift für Phys., vol. 54, no. 7–8, pp. 537–563, 1929.

[43] F. F. Grinstein, "Vortex dynamics and entrainment in rectangular free jets," J. Fluid Mech., vol. 437, pp. 69–101, 2001.

[44] L. Talbot, R. K. Cheng, R. W. Schefer, and D. R. Willis, "Thermophoresis of particles in a heated boundary layer," J. Fluid Mech., 1980.

[45] J. M. Gorman, E. M. Sparrow, and J. P. Abraham, "Slot jet impingement heat transfer in the presence of jet-axis switching," Int. J. Heat Mass Transf., 2014.

[46] M. Jadidi, M. Mousavi, S. Moghtadernejad, and A. Dolatabadi, “A Three-Dimensional Analysis of the Suspension Plasma Spray Impinging on a Flat Substrate,” J. Therm. Spray Technol., 2014.